

**RL-TR-97-48**  
Final Technical Report  
July 1997



# **USE OF BALLISTIC-ELECTRON-EMISSION MICROSCOPY TO STUDY MECHANISMS FOR LONG WAVELENGTH SCHOTTKY- BARRIER INFRARED DETECTORS**

Rensselaer Polytechnic Institute

Leo J. Schowalter

*APPROVED FOR PUBLIC RELEASE; DISTRIBUTION UNLIMITED.*

**19970929 016**

*DIGITAL QUALITY INSPECTED 4*

**Rome Laboratory  
Air Force Materiel Command  
Rome, New York**

This report has been reviewed by the Rome Laboratory Public Affairs Office (PA) and is releasable to the National Technical Information Service (NTIS). At NTIS it will be releasable to the general public, including foreign nations.

RL-TR-97-48 has been reviewed and is approved for publication.

APPROVED:

*Jerry Silverman*

JERRY SILVERMAN

Project Engineer

FOR THE COMMANDER:

*Simeon D. Breault*

SIMEON D. BREAULT, Lt Col, USAF

Deputy Director

Electromagnetics & Reliability Directorate

If your address has changed or if you wish to be removed from the Rome Laboratory mailing list, or if the addressee is no longer employed by your organization, please notify RL/EROI, 80 Scott Dr., Hanscom AFB MA 01731-2909. This will assist us in maintaining a current mailing list.

Do not return copies of this report unless contractual obligations or notices on a specific document require that it be returned.

REPORT DOCUMENTATION PAGE			Form Approved OMB No. 0704-0188
<p>Public reporting burden for this collection of information is estimated to average 1 hour per response, including the time for reviewing instructions, searching existing data sources, gathering and maintaining the data needed, and completing and reviewing the collection of information. Send comments regarding this burden estimate or any other aspect of this collection of information, including suggestions for reducing this burden, to Washington Headquarters Services, Directorate for Information Operations and Reports, 1215 Jefferson Davis Highway, Suite 1204, Arlington, VA 22202-4302, and to the Office of Management and Budget, Paperwork Reduction Project (0704-0188), Washington, DC 20503.</p>			
1. AGENCY USE ONLY (Leave blank)	2. REPORT DATE	3. REPORT TYPE AND DATES COVERED	
	July 1997	Final Jun 93 - Jun 96	
4. TITLE AND SUBTITLE		5. FUNDING NUMBERS	
USE OF BALLISTIC-ELECTRON-EMISSION MICROSCOPY TO STUDY MECHANISMS FOR LONG WAVELENGTH SCHOTTKY-BARRIER DETECTORS		C - F19628-93-K-0015 PE - 62702F PR - 4600 TA - 18 WU - 20	
6. AUTHOR(S)			
Leo J. Schowalter			
7. PERFORMING ORGANIZATION NAME(S) AND ADDRESS(ES)		8. PERFORMING ORGANIZATION REPORT NUMBER	
Rensselaer Polytechnic Institute Troy, NY 12180		N/A	
9. SPONSORING/MONITORING AGENCY NAME(S) AND ADDRESS(ES)		10. SPONSORING/MONITORING AGENCY REPORT NUMBER	
Rome Laboratory/EROI 80 Scott Dr. Hanscom AFB, MA 01731-2909		RL-TR-97-48	
11. SUPPLEMENTARY NOTES			
Rome Laboratory Project Engineer: Jerry Silverman/EROI/617-377-3295			
12a. DISTRIBUTION AVAILABILITY STATEMENT		12b. DISTRIBUTION CODE	
Authorized for public release; distribution unlimited.			
13. ABSTRACT (Maximum 200 words)			
<p>In this final report, we have summarized our work in five areas. The first area, covered in Sec. I, is the development of calcium fluoride tunnel barriers which may be used to increase the operating temperature of PtSi SBIRDs. In particular, we have demonstrated a new technique for growth of exactly two monolayers of CaF<sub>2</sub> on Si(111) substrates. In Sec. II, we describe our work with ballistic electron emission microscopy to determine electron scattering processing in thin metal layers and at metal/Si interfaces. During this contract, we constructed an in-situ STM/BEEM system which allowed us to make measurements directly on PtSi and Pt surfaces without having to protect these surfaces from oxidation. Our preliminary results with this instrument are described in Sec. III. Sec. IV describes the theoretical model we have developed which explains why the Fowler-like behavior typically observed in the photoresponse for many Schottky-barrier metal/semiconductor interfaces does not prove that crystal momentum parallel to the interface is conserved. In Sec. V, we describe the Monte-Carlo program that we have developed to model ballistic electron scattering in this metal layers and across the metal/semiconductor interface. Initial results demonstrate that electron (or hole) scattering at the metal/semiconductor interface may, in fact, be the dominant transmission mechanism for most (nonpitaxial) metal/semiconductor systems.</p>			
14. SUBJECT TERMS		15. NUMBER OF PAGES	
Infrared detectors, Schottky-barrier, Metal/semiconductor Ballistic-electron-emission microscopy (BEEM), Scanning tunneling microscopy (STM), epitaxial insulator, atomic steps, calcium fluoride.		52	
16. PRICE CODE			
17. SECURITY CLASSIFICATION OF REPORT	18. SECURITY CLASSIFICATION OF THIS PAGE	19. SECURITY CLASSIFICATION OF ABSTRACT	20. LIMITATION OF ABSTRACT
UNCLASSIFIED	UNCLASSIFIED	UNCLASSIFIED	UL

## TABLE OF CONTENTS

SECTION	PAGE
I. CALCIUM FLUORIDE TUNNEL BARRIERS	1
II. MEASUREMENT OF HOT-ELECTRON SCATTERING PROCESSES AT SCHOTTKY INTERFACES BY TEMPERATURE-DEPENDENT BALLISTIC ELECTRON EMISSION MICROSCOPY	10
IIA. Introduction	10
IIB. Hot-Electron Scattering Processes	12
IIC. Experimental	14
IID. Results	15
IID.1 Temperature-Dependent BEEM Spectroscopy	15
IID.2 Room Temperature BEEM Imaging	16
III. Discussion	17
IIF. Conclusions	19
III. DESIGN AND INSTALLATION OF A SCANNING TUNNELING MICROSCOPE FOR <i>IN-SITU</i> TOPOGRAPHIC AND SPECTROSCOPIC/BEEM MEASUREMENTS WITHIN OUR MOLECULAR BEAM EPITAXY MACHINE	28
IV. CONSERVATION OF MOMEMTUM PARALLEL OF THE INTERFACE	34
V. MONTE-CARLO CALCULATIONS OF BALLISTIC ELECTRON SCATTERING	35

## LIST OF FIGURES

FIGURE	PAGE	
1	(a) The specular diffraction spot RHEED intensity profile monitored during a $5.2 \pm 0.7$ -nm-thick $\text{CaF}_2$ epitaxy on the $0.5^\circ$ miscut $\text{Si}(111)$ substrate at $770^\circ\text{C}$ . The RHEED intensity profile initially shows almost two oscillations which correspond to 2 MLs of layer-by-layer $\text{CaF}_2$ growth. (b) The average $\text{CaF}_2$ film thickness determined by RHEED ( $d_{\text{RHEED}}$ ) is plotted as a function of the average $\text{CaF}_2$ film thickness determined by RBS ( $d_{\text{RBS}}$ ). The $\text{CaF}_2$ thickness, $d_{\text{RHEED}}$ , was measured by associating the second peak of oscillations in the RHEED intensity profile with 2 MLs for the $\text{CaF}_2$ films grown at $770^\circ\text{C}$ .	5
2	Four AFM images are shown, which characterize the evolution of $\text{CaF}^2$ surface morphology when the films are grown on $2^\circ$ vicinal substrates at $770^\circ\text{C}$ . In (a), the average $\text{CaF}_2$ film thickness $t$ is $0.5 \pm 0.2$ nm while the AFM height range $r$ in the image is 5 nm. In (b), $t=0.8 \pm 0.3$ nm and $r=15$ nm. In (c), $t=2.5 \pm 0.5$ nm and $r=15$ nm. In (d), $t=5.2 \pm 0.7$ nm and $r=30$ nm.	6
3	The average $\text{CaF}_2$ thickness $d_B$ (as measured by RBS) is plotted versus the fraction $f$ (as measured by AFM) of the wetting layer covered by thick $\text{CaF}_2$ islands for $2^\circ$ ( <b>open circle</b> ) and $0.5^\circ$ ( <b>solid circle</b> ) miscut $\text{Si}(111)$ substrates.	7
4	An AFM image is shown, which characterizes the surface morphology of a $5.2 \pm 0.7$ -nm-thick $\text{CaF}_2$ grown at $770^\circ\text{C}$ on a $0.1^\circ$ miscut $\text{Si}(111)$ substrate.	8
5	A series of J-V curves that were taken at room T on $\text{CaF}_2$ films of various thickness grown at $770^\circ\text{C}$ on (a) $2^\circ$ miscut and (b) $0.1^\circ$ miscut $\text{Si}(111)$ substrates are shown. The inset figure within (b) is a plot of $J$ at 1 V as a function of $\text{CaF}_2$ film thickness for $2^\circ$ ( <b>open circle</b> ) and $0.1^\circ$ ( <b>closed circle</b> ) miscut substrates.	9
6	Schematic of Beem electron transport across a metal-semiconductor Schottky interface (not drawn to scale). For electrons injected into the metal overlayer with a tip bias greater than the Schottky barrier, $\Phi_S$ , a fraction of the injected electrons will travel across the barrier and be detected as a BEEM electron. The magnitude of the BEEM current is strongly influenced by scattering processes in the metal overlayer, at the metallurgical interface, and within the semiconducting substrate.	22

## LIST OF FIGURES, Continued

FIGURE	PAGE	
7	Semilog plot of BEEM transmittances, $I_B/I_T \times 100$ , at a tip bias of -1.2 V measured on several Au/Si(100) samples at 77 K (circles) and RT (squares). A minimum of 80 spectra were collected at each coverage and temperature. The linear curves through the data sets represents least-squares fits applied to the data. From the slope and intercept of these curves, the attenuation length of the electrons in the Au overlayer, $\lambda_a$ , and the zero thickness transmittance, $I_o$ , are determined.	23
8	(a) Plot of the ratio of the zero thickness transmittance at 77 K to that at RT, $I_o(77K)/I_o(RT)$ , as a function of kinetic energy, $eV_T - \Phi_S$ , in the semiconductor. An average value of $1.79 \pm 0.09$ over the kinetic energy range of 140 meV to 380 meV is obtained for $I_o(77K)/I_o(RT)$ . (b) Plot of the attenuation length of the BEEM electrons in the Au overlayer at both 77 K (circles) and RT (squares) as a function of tip bias. Only a slight temperature dependence to $\lambda_a$ is observed, $\lambda_a$ (300K) = $133 \pm 2$ Å and $\lambda_a$ (77K) = $147 \pm 6$ Å. Within the experimental uncertainty of these measurements, no energy dependence of $\lambda_a$ is observed.	24
9	Calculation of the reduction of normalized BEEM current, $I_B(\theta)/I_B(0^\circ)$ , that results from the increase in path length to the M-S interface for non-zero injection angles for several metal overlayer thicknesses. This calculation assumes that any electron reaching the M-S interface is equally likely to cross it regardless of its momentum parallel to the interface.	25
10	Schematic of the effect of tip apex geometry on the resolved topography (dashed lines) of the STM and the injection angle of the electrons. (a) Imaging with a tip apex which has a radius of curvature larger than the actual topographic features of the surface will result in an inability to resolve the surface regions with large gradients, e.g. the crevices between the rounded surface structures, (b) Imaging with a tip which has a sharp "mini tip" which is longer than the average corrugation height of the surface will result in a measured topography which closely mimics the actual topography.	26

## LIST OF FIGURES, Continued

FIGURE		PAGE
11	(a) STM topographic image of a ~500 Å x ~500 Å area of a 103 Å Au/Si(100) sample ( $V_T = -1.2V$ and $I_T = 5\text{ nA}$ ). (b) BEEM image taken simultaneously with the topographic image shown in (a). The grey scale range for the BEEM image is 0-120 pA with dark areas representing low BEEM current. The grey scale range for the STM image is 120 Å with light areas representing high surface features. Surface gradients as high as ~75° are observed in the STM image and correlate to regions of the BEEM image with an ~85% reduction in the BEEM current.	27
12	Schematic of the side view of the preparation chamber of the V90H MBE machine with the wafer-STM installed. The STM design uses two Burleigh inchworms: one which has a scanner tube for STM measurements and a second with an electrode which is used to make a front contact for BEEM measurements. The STM incorporates a push-pull device to allow the transfer of wafers through the preparation chamber to the deposition chamber. The diameter of the preparation chamber is 15 inches and the distance from the STM support flange to the preparation chamber center line is 25 inches.	29
13	Constant current topographic image of the 7x7 Si(111) surface taken with all of the system's pumps in operation ( $I_{tip} = 1\text{ nA}$ , $V_{tip} = 2V$ ).	30
14	Averaged BEEM spectrum for a 2 nm PtSi/Si(111) n-type interface ( $I_{tip} = 1\text{ nA}$ ).	31
15	Averaged BEEM spectrum for a 2 nm Pt/ 0.6 nm CaF <sub>2</sub> / Si(111) n-type interface ( $I_{tip} = 1\text{ nA}$ ). Note that the spectrum appears to show resonant tunneling at a tip bias of -1.8 V which is below the CaF <sub>2</sub> conduction band at -3.5 V (i.e. 3.5 eV above the Pt Fermi energy).	32
16	STM image of the 2 nm Pt/0.6 nm CaF <sub>2</sub> /Si(111) surface showing the nodules of Pt that appear on the as-deposited surface. In addition, the atomic steps in the underlying CaF <sub>2</sub> are clearly visible.	33
17	Three different MC calculations of the BEEM current.	37
18	The natural log of the total BEEM current is plotted as a function of metal thickness while the tip bias is held constant at -1.2V and the tip separation is fixed at 0.5 nm. The apparent nonlogarithmic behavior of the BEEM current at thin metal thickness is due to electrons being able to rattle back and forth between the front and m/s interfaces.	38

This contract was for us to improve the understanding of internal photoemission for Schottky-barrier IR detectors (SBIRDs) and to attempt to use this improved understanding to design either more efficient SBIRDs or SBIRDs with improved wavelength of operation or to increase the operating temperature. Below, we have summarized our work in five areas on this project. The first area, covered in Sec. I, is the development of calcium fluoride tunnel barriers which may be used to increase the operating temperature of PtSi SBIRDs. In particular, we have demonstrated a new technique for growth of exactly two monolayers of CaF<sub>2</sub> on Si(111) substrates. In Sec. II, we describe our work with ballistic electron emission microscopy to determine electron scattering processes in thin metal layers and at metal/Si interfaces. During this contract, we constructed an *in-situ* STM/BEEM system which allowed us to make measurements directly on PtSi and Pt surfaces without having to protect these surfaces from oxidation. Our preliminary results with this instrument are described in Sec. III. Sec. IV describes the theoretical model we have developed which explains why the Fowler-like behavior typically observed in the photoresponse for many Schottky-barrier metal/semiconductor interfaces does not prove that crystal momentum parallel to the interface is conserved. In fact, it is more likely an indicator that scattering at the interface dominates and crystal momentum is not a good quantum number at all. Finally, in Sec. V, we describe the Monte-Carlo program that we have developed to model ballistic electron scattering in thin metal layers and across the metal/semiconductor interface. Initial results demonstrate that electron (or hole) scattering at the metal/semiconductor interface may, in fact, be the dominant transmission mechanism for most (nonepitaxial) metal/semiconductor systems.

Details of papers published, presentations, meeting attendance, and interactions are given at the end of this report.

## I. Calcium fluoride tunnel barriers

### Summary of this work:

A new technique for growth of exactly two monolayers of CaF<sub>2</sub> on Si(111) substrates is demonstrated. This technique takes advantage of the tendency of CaF<sub>2</sub> to form thick islands at Si step edges on vicinal substrates once a two-monolayer thick wetting layer is deposited. A comparison of I-V characteristics for epitaxial CaF<sub>2</sub> layers grown on on-axis versus off-axis substrates demonstrates the advantages of this technique. This technique has potential application for tunnel barriers and other applications where precise control of the thickness of a very thin layer is crucial. In particular, we believe that these tunnel barriers can be used to reduce the ratio of dark current to signal at higher operating temperatures for Schottky-barrier IR detectors (SBIRDs).

For these studies, thin CaF<sub>2</sub> films were grown at 770 °C by molecular beam epitaxy on Si(111)-(7x7) substrates which were miscut by either ~2°, ~0.5°, or ~0.1° toward the<sup>11-2</sup> azimuth. Prior to growth, the substrates were prepared by a standard RCA chemical clean followed by a heat cleaning to 975 °C for 35 minutes in the MBE growth chamber; further details are given in Refs. 6 and 7. The surface of the epitaxial CaF<sub>2</sub> films was characterized *in-situ* with reflection high energy electron diffraction (RHEED), using 14 keV electrons, and *ex-situ* with atomic force microscopy (AFM). The average thickness of films was determined by Rutherford

backscattering spectrometry (RBS) using 2 MeV He<sup>+</sup> ion beam. Metal-insulator-semiconductor structures were prepared for I-V measurements by evaporating Au dots ( $7 \times 10^{-2}$  cm<sup>2</sup> in area and ~100 nm in thickness) through a shadow mask onto the epitaxial CaF<sub>2</sub> layers, by using a resistively heated Tungsten boat placed in a conventional, high vacuum chamber.

A typical RHEED intensity temporal profile, monitored during CaF<sub>2</sub> growth at 770 °C, is shown in Fig. 1a. After CaF<sub>2</sub> deposition is initiated, the specular diffraction spot RHEED intensity shows almost two complete oscillations which indicates that the single step density oscillates as monolayer-high islands nucleate and then coalesce<sup>3</sup>. After the second peak, the RHEED intensity decays gradually to a constant level indicating that the step density approaches a constant value as further CaF<sub>2</sub> growth proceeds. The CaF<sub>2</sub> flux was determined *in-situ* by associating the second peak in the RHEED intensity profile with 2 monolayers (MLs) of CaF<sub>2</sub> deposition. This assumption was verified by demonstrating that the average CaF<sub>2</sub> film thickness determined by RHEED  $d_{\text{RHEED}}$  corresponded very well to the average CaF<sub>2</sub> film thickness determined by Rutherford backscattering spectrometry (RBS)  $d_{\text{RBS}}$  as shown in Fig. 1b.

The surface morphology (Fig. 2a) of a  $0.5 \pm 0.2$ -nm-thick CaF<sub>2</sub> film grown at 770 °C on the 2° miscut Si substrate exhibits random corrugations, which have an average height of  $0.45 \pm 0.1$  nm and a diameter of  $30 \pm 15$  nm, over the entire Si surface. This result is consistent with the oscillations in the RHEED intensity observed at the initiation of epitaxy and indicates that the wetting layer grows by formation and coalescence of isolated islands of atomic height on the Si terraces. Under these growth conditions, similar findings have been reported by Tromp et al.<sup>4</sup> using *in-situ* low energy electron microscopy (LEEM) and also by Avouris et al.<sup>5</sup> using ultra-high vacuum, scanning tunneling microscopy. CaF (layer 1) and CaF<sub>2</sub> (layer 2)

The evolution of CaF<sub>2</sub> surface morphology observed beyond 2 MLs (for the CaF<sub>2</sub> films grown at 770 °C on 2° miscut substrates) as characterized by AFM is illustrated in Figs. 2b to 2d. It shows that thick islands (in triangular shapes with an average height of ~5 nm) are nucleated at the Si step edges which are bunched into step bands with an average height of ~3 nm (Fig. 2b). These islands grow laterally (in trapezoidal shapes) along the step bands (Fig. 2c) until they coalesce and form a complete overlayer after ~5.2 nm of CaF<sub>2</sub> is deposited (Fig. 2d).

The plot shown in Fig. 3 summarizes the early stages of CaF<sub>2</sub> epitaxy at 770 °C on both 2° and 0.5° miscut Si (111) substrates. By linearly fitting the data points in the plot, we have extracted a simple equation of the form:

$$d_B = d_C + d_I \cdot f, \quad (1)$$

where  $d_B$  corresponds to the average CaF<sub>2</sub> thickness (as determined by RBS),  $f$  corresponds to the fraction of area covered by CaF<sub>2</sub> islands (as determined by AFM),  $d_C$  and  $d_I$  are fitting parameters corresponding to the wetting layer thickness and the average island height, respectively. For 2° miscut substrate, the best-fit values of  $d_I = 5.19$  nm and  $d_C = 0.54$  nm were determined while corresponding fit values on the 0.5° miscut substrate were:  $d_I = 1.91$  nm and  $d_C = 0.21$  nm. This linear relationship between  $f$  and  $d_B$  demonstrates an unusual growth behavior after the CaF<sub>2</sub> wetting layer ( $d_C$ ) is formed. Thick island nucleation occurs in triangular shapes at the step bands only after this wetting layer is formed. Remarkably, once nucleated, the thick islands grow laterally along the step bands with a constant island height ( $d_I$ ) to eventually form a flat overlayer (i.e.,  $d_B = d_C + d_I$  at  $f=1$ ). In agreement with this simple picture, we find that the CaF<sub>2</sub> uniformly covers the entire surface when the total layer thickness exceeds 5.73 nm or 2.12 nm on vicinal substrates miscut by 2° or 0.5°, respectively.

The specular diffraction spot RHEED intensity profile, monitored during  $\text{CaF}_2$  epitaxy on well oriented ( $< 0.1^\circ$  miscut) substrates, indicates that the growth proceeds in a layer-by-layer mode up to 2 MLs in the same fashion as nucleation observed on both  $0.5^\circ$  and  $2^\circ$  miscut substrates. However, unlike the vicinal substrates, growth beyond the first 2-MLs proceeds in a step flow fashion without the formation of thick islands. Furthermore, we observe the onset of line-defect formations, characteristic of misfit dislocations, for films thicker than 3 nm. On the somewhat thicker layer for a total thickness of a  $5.2 \pm 0.7$  nm, evidence for a regular array of misfit dislocations, which densified with film thickening, is observed (Fig. 4). Almost identical misfit-dislocation configurations have also been reported by Tromp et al.<sup>4</sup> who studied the strain relaxation mechanism by following the growth of  $\text{CaF}_2$  at  $770^\circ\text{C}$  on well-oriented Si(111) substrates with in-situ LEEM.

Figs. 5a and 5b Show a series of current density-voltage (J-V) curves taken on the  $\text{CaF}_2$  layers of various film thickness grown on  $2^\circ$  miscut and  $0.1^\circ$  miscut Si(111) substrates, respectively. Looking at the shape of the J-V curves., one can see that, on  $2^\circ$  miscut substrates, the current density progressively shifts downward in correspondence with increasing film thickness. This point is highlighted in the inset (marked as **open circles**) of Fig. 5b, a plot of  $J$  at 1 V for different values of film thickness, which illustrates the current reduction of an approximately two orders of magnitude between the thinnest (0.5 nm) and thickest (5.2 nm) films grown on  $2^\circ$  miscut substrates. On the other hand, as shown in Fig. 5b, a completely different conduction behavior is observed for films grown on  $0.1^\circ$  miscut substrates in which the J-V curve of a 2.7 nm thick film lies below that of the thinnest film (0.8 nm), while for thicker films (3.4 nm and 5.2 nm) the curves are positioned above that of the thinnest film. This point is also highlighted in the inset (marked as **closed circles**) of Fig. 5b which shows the initial decrease followed by subsequent increase in the current density with film thickening.

The electrical results in Figs. 5 have a strong correspondence with our AFM data which demonstrated the onset of dislocation nucleation at critical thickness of  $\sim 3$  nm for films grown on  $0.1^\circ$  miscut substrates, while line-defect free terraces were observed up to 9 nm for films grown on  $2^\circ$  miscut substrates. Under an assumption that the 2.7 nm thick film in Fig. 5b is coherently strained, the current conduction in the film is expected to be smaller than that of the 0.8 nm thick film. However, upon crossing the critical thickness at  $\sim 3$  nm, misfit dislocations are nucleated at the interface, which may provide a pathway for the larger current flow in films thicker than 3 nm. It should be also noted that the current flow in films thicker than 3 nm grown on  $2^\circ$  miscut substrates is approximately two orders of magnitude smaller than for films grown on  $0.1^\circ$  miscut substrates. The J-V trend on  $2^\circ$  miscut substrates may represent epitaxial films which are largely made up of coherent structures, and the misfit dislocations and increased defect concentration in the relaxed films of  $0.1^\circ$  miscut substrates may allow for the larger current conduction than in the apparent, pseudomorphic films of  $2^\circ$  miscut substrates, as observed in Figs. 5.

In conclusion, we have shown that at  $770^\circ\text{C}$  on clean Si(111) 7x7 surfaces,  $\text{CaF}_2$  first forms a 2-MLs-thick wetting layer, which exhibit a rough surface, in a layer-by-layer mode. However, subsequent growth beyond 2 MLs depends strongly on substrate misorientation. On vicinal substrates,  $\text{CaF}_2$  growth proceeds by the nucleation and coalescence of apparent, pseudomorphic islands at Si step bunches. While on well oriented substrates,  $\text{CaF}_2$  grows rather uniformly without forming thick islands. In this case, misfit strain is apparently relieved by nucleating dislocations with critical thickness at  $\sim 3$  nm.

## **References for Section I**

- [1] L. J. Schowalter and R. W. Fathauer, CRC Cri. Rev. **15**, 367 (1989).
- [2] T. Suemasu, M. Watanabe, J. Suzuki, Y. Kohno, M. Asada, and N. Suzuki, J. Appl. Phys. **33**, 57 (1994).
- [3] J. H. Neave, P. J. Dobson, B. A. Joyce, and Jing Zhang, Appl. Phys. Lett. **47**, 102 (1985).
- [4] R. M. Tromp, F. K. LeGoues, and M. C. Reuter, Phys. Rev. Lett. **74**, 2706 (1995).
- [5] Ph. Avouris and R. Wolkow, Appl. Phys. Lett. **55**, 1074 (1989).
- [6] Applied Surface Science Paper (ICFSI Conf. paper)?
- [7] B.M. Kim, Ph.D. Thesis (Rensselaer Polytechnic Institute, unpublished, 1996).

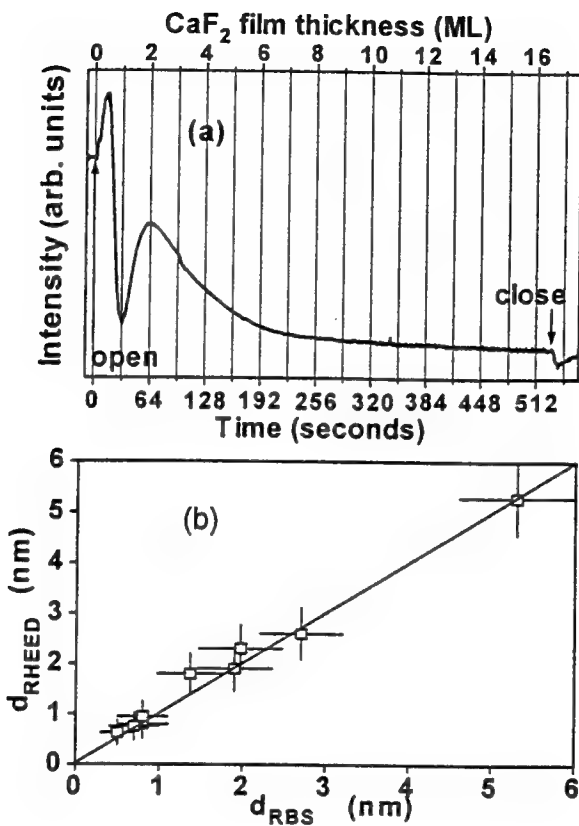


Fig. 1. (a) The specular diffraction spot RHEED intensity profile monitored during a  $5.2 \pm 0.7$ -nm-thick CaF<sub>2</sub> epitaxy on the 0.5° miscut Si(111) substrate at 770 °C. The RHEED intensity profile initially shows almost two oscillations which correspond to 2 MLs of layer-by-layer CaF<sub>2</sub> growth. (b) The average CaF<sub>2</sub> film thickness determined by RHEED ( $d_{\text{RHEED}}$ ) is plotted as a function of the average CaF<sub>2</sub> film thickness determined by RBS ( $d_{\text{RBS}}$ ). The CaF<sub>2</sub> thickness,  $d_{\text{RHEED}}$ , was measured by associating the second peak of oscillations in the RHEED intensity profile with 2 MLs for the CaF<sub>2</sub> films grown at 770 °C.

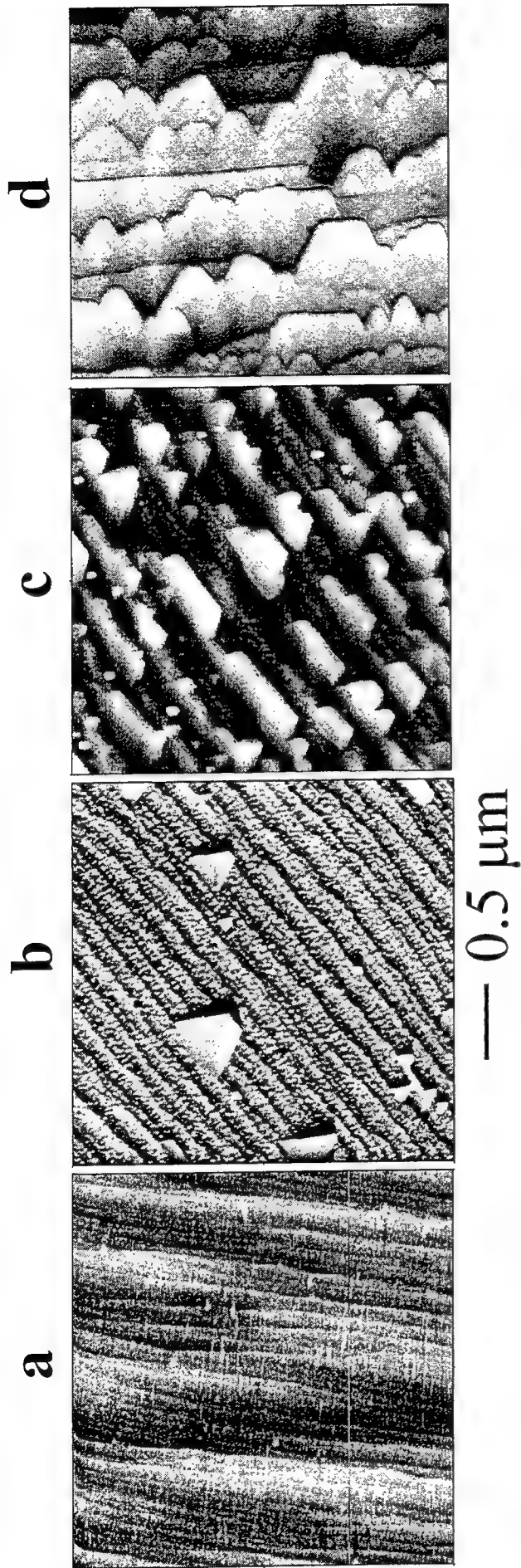


Fig. 2. Four AFM images are shown, which characterize the evolution of  $\text{CaF}_2$  surface morphology when the films are grown on  $2^\circ$  vicinal substrates at  $770^\circ\text{C}$ . In (a), the average  $\text{CaF}_2$  film thickness  $t$  is  $0.5\pm0.2$  nm while the AFM height range  $r$  in the image is 5 nm. In (b),  $t=0.8\pm0.3$  nm and  $r=15$  nm. In (c),  $t=2.5\pm0.5$  nm and  $r=15$  nm. In (d),  $t=5.2\pm0.7$  nm and  $r=30$  nm.

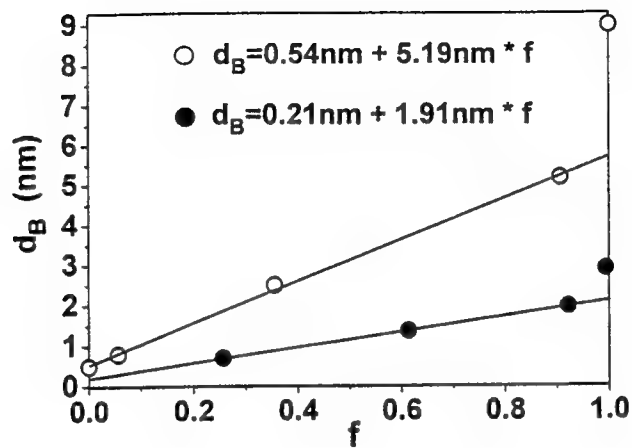


Fig. 3. The average  $\text{CaF}_2$  thickness  $d_B$  (as measured by RBS) is plotted versus the fraction  $f$  (as measured by AFM) of the wetting layer covered by thick  $\text{CaF}_2$  islands for  $2^\circ$  (open circle) and  $0.5^\circ$  (solid circle) miscut  $\text{Si}(111)$  substrates.

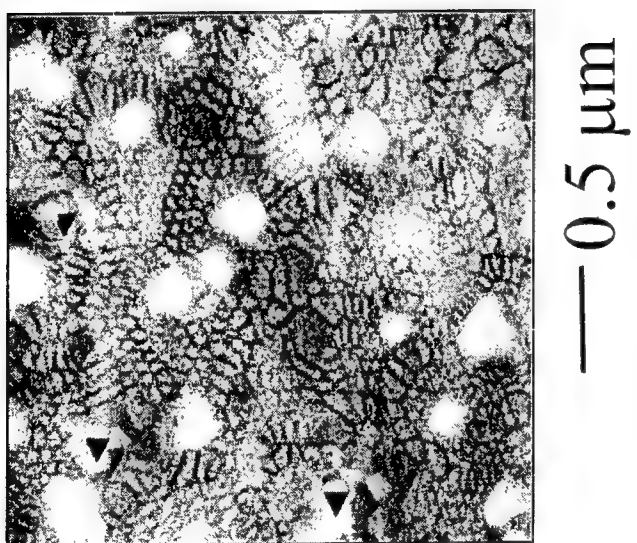


Fig. 4. An AFM image is shown, which characterizes the surface morphology of a  $5.2 \pm 0.7$ -nm-thick  $\text{CaF}_2$  grown at  $770^\circ\text{C}$  on a  $0.1^\circ$  miscut  $\text{Si}(111)$  substrate.

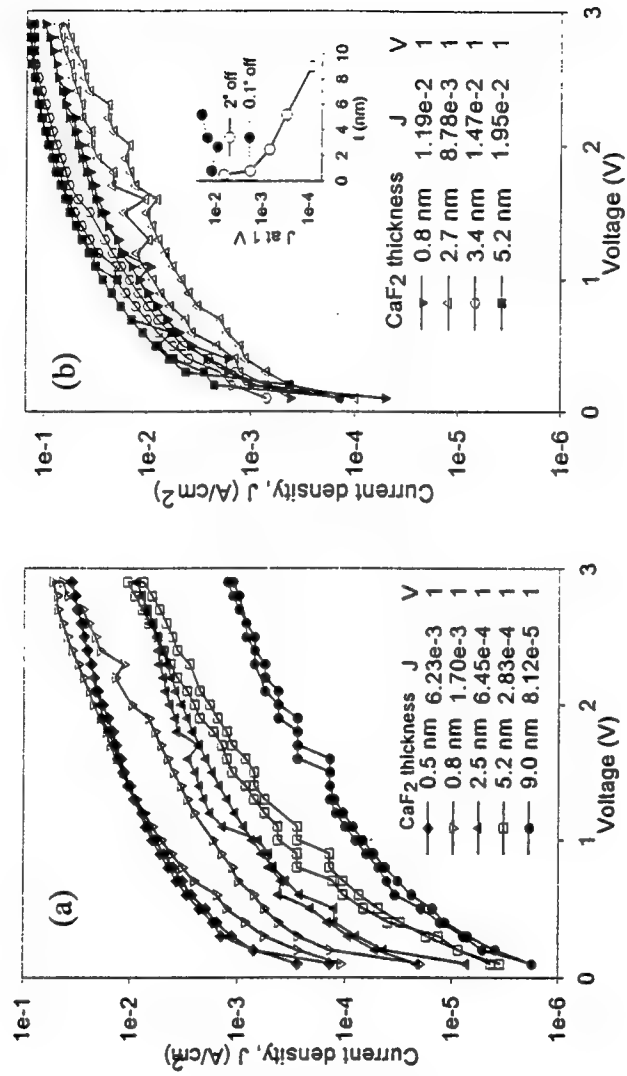


Fig. 5 A series of J-V curves that were taken at room T on CaF<sub>2</sub> films of various thickness grown at 770°C on (a) 2° miscut and (b) 0.1° miscut Si(111) substrates are shown. The inset figure within (b) is a plot of J at 1 V as a function of CaF<sub>2</sub> film thickness for 2° (open circle) and 0.1° (closed circle) miscut substrates.

## **II. Measurement of Hot-Electron Scattering Processes at Schottky Interfaces by Temperature-Dependent Ballistic Electron Emission Microscopy**

Summary of this work:

Ballistic electron emission microscopy measurements have been performed on n-type Au/Si(100) interfaces for injection energies up to 1.2 eV over a range of Au overlayer thicknesses from ~65 Å to ~340 Å at both room temperature and 77 K. Hot-electron attenuation lengths in the Au overlayer have been determined to be  $133 \pm 2$  Å at room temperature and  $147 \pm 6$  Å at 77 K over the energy range of 0.92 eV to 1.20 eV above the Fermi level. The lack of energy dependence and the relatively small temperature-dependent change in the attenuation lengths that have been measured indicate that electron scattering with defects is the dominant mechanism affecting hot-electron transport in these Au overlayers. The ratio of the zero thickness collection current at 77 K to that at room temperature has been measured to be  $1.79 \pm 0.09$ . This large increase in the collection efficiency at 77 K is attributed primarily to the large temperature dependence of the transverse acoustic phonon population in Si. Images with significant reductions in the collection current at topographic locations which have a large surface gradient have been obtained at room temperature. Calculations, which assume that the probability of transmission across the interface is independent of the transverse momentum of the electron, correlate well with the experimentally observed reductions. This result indicates that the injected electrons remain forward focused with little broadening as they pass through the Au overlayer which implies that elastic scattering at the Au/Si interface accounts for the observation from previous Au/Si ballistic electron emission microscopy studies that transverse momentum is not conserved.

### *IIA. Introduction*

A fundamental understanding of the various hot-electron scattering processes at metal-semiconductor (M-S) interfaces is important for the optimization of the transport properties of many electronic devices such as metal-base transistors and infrared Schottky photodiodes. During the initial stages of the development of solid-state technology in the 1960's, there was a considerable research effort in this field. The primary experimental method which was used to measure the scattering lengths of hot-electrons in metals during that time was internal photoemission<sup>1</sup>. This technique measures the photoresponse of a M-S interface over a series of metal film thicknesses to determine the attenuation length,  $\lambda_a$ , of the photoexcited electrons. However, extracting the path length for inelastic scattering from this data is complicated by the fact that the penetration depth of the photons in the metal as well as the energy distribution of the photoexcited electrons is dependent on the photon energy. In addition, the kinetic energy range over which  $\lambda_a$  can be measured is limited to the band gap,  $E_g$ , of the semiconductor. The uncertainty in these early internal photoemission measurements is exemplified by the fact that values of  $\lambda_a$  ranging from 740 Å to 330 Å at a photon energy of ~1 eV have been reported for Au/Si samples by different research groups<sup>2-4</sup>.

The development of ballistic electron emission microscopy (BEEM) by Bell and Kaiser<sup>5</sup> has provided the scientific community with a powerful new tool for determining hot-electron scattering lengths at M-S interfaces. BEEM is a scanning tunneling microscopy (STM) based

technique where the STM tip is used as a very narrow, energy-tunable, forward-focused source for electron injection into a metal overlayer. By collecting the current which passes through the metal into the semiconductor as a function of tip position and tip bias, information about the local Schottky barrier height and the hot-electron transport properties can be obtained on a nanometer scale. However, to properly interpret the spectroscopy data and interfacial images obtained with BEEM, a fundamental understanding of the scattering process within the metal overlayer, at the metallurgical interface, and within the Si substrate is essential. In this paper, we report BEEM measurements which were performed to determine the relative importance of temperature-dependent scattering mechanisms on hot-electron transport across Au/Si(100) interfaces. The Au/Si system was chosen as a model M-S interface primarily because of the relatively simple electronic structure of Au, a lone 6s electron in its outer shell and a filled inner 5d shell. In addition, Au is a noble metal which provides an advantage over most metals in that it can be characterized under ambient conditions.

Although Au/Si has been the most thoroughly studied interface with the BEEM technique, it has also proved to be one of the most controversial interfaces. In the first BEEM studies of Au/Si(100) by Bell and Kaiser<sup>5</sup>, excellent agreement was obtained between their spectroscopy data and calculated curves which were derived assuming ballistic transport through the metal overlayer and transverse momentum conservation at the interface. However, Schowalter and Lee<sup>6</sup> made the observation that the BEEM spectra for both the Si(100) and Si(111) substrates have similar line shapes and current onsets which is unexpected since transport into the Si(111) surface requires a large transverse crystal momentum component while transport into the Si(100) surface does not. Monte Carlo simulations of the BEEM spectra using a model which conserves transverse momentum at the M-S interface were performed and indicated that elastic scattering in the Au overlayers, accompanied by multiple reflections off the surface and interface, resulted in a near isotropic momentum distribution and an inherent loss of spatial resolution at the M-S interface. A subsequent BEEM study by Lee et al.<sup>7</sup> which found no correlation between surface gradients and the measured BEEM current gave support to these Monte Carlo calculations. In contrast to these results, a BEEM study by Palm, Arbes and Schulz<sup>8</sup> which directly imaged fluctuations in the Schottky barrier height of Au/Si(100) interfaces over spatial distances of ~15 Å provides evidence that transport through the metal overlayer is essentially ballistic.

To complicate matters further, a microscopy study by Fernandez *et al.*<sup>9</sup> found that for Au/Si interfaces grown under ultra-high vacuum (UHV) conditions on bare Si and imaged in air, no BEEM current could be detected. They interpreted the lack of BEEM current to the formation of a disordered Au-Si alloy at the interface which resulted in strong scattering of the BEEM electrons. In addition, they found that by controllably dosing the clean Si surface with various gas molecules before Au deposition they could obtain homogeneous BEEM currents that could be irreversibly changed by performing BEEM at tip biases higher than ~3 V. However, a recent BEEM study by Cuberes *et al.*<sup>10</sup> of Au/Si(111) samples prepared and imaged under UHV conditions found that BEEM currents could be obtained at tip biases as large as 8 eV with no apparent modification of the interface. Their synchrotron based photoelectron spectroscopy (PES) results also indicated that the Au/Si interface formed at room temperature (RT) is an abrupt interface with a silicide-like surface segregation layer. Trying to reconcile these results is difficult due to differences in sample preparation conditions and in the methods of detection used by many of the groups performing BEEM research.

Although the experimental evidence<sup>6,11</sup> for non-conservation of transverse momentum is quite strong for Au/Si and Pd/Si interfaces, the precise nature of the scattering mechanisms is not well understood. It would seem that symmetry breaking parallel to the interface would be a sufficient condition for violation of transverse momentum conservation since these are non-epitaxial systems. On the other hand, microscopy and spectroscopy studies<sup>12,13</sup> of Au/GaP(110) and Mg/GaP(110) which are non-epitaxial and also non-abrupt interfaces have obtained good agreement between curves fitted with a transverse momentum conserving model and their experimental data. Presently, it is not clear whether these discrepancies result from an additional source of scattering that may be present at Au/Si and Pd/Si interfaces or from the method which was used to model the data for the Au/GaP(110) and Mg/GaP(110) studies.

To better understand the scattering mechanisms at Au/Si interfaces, we have performed a temperature-dependent BEEM spectroscopy and RT BEEM microscopy study on the Au/Si(100) interface. Our spectroscopy data indicate that there is a large temperature dependence to the measured BEEM transmittance yet only a small temperature-dependent change in the attenuation length of the electrons in the Au overayers. From these results, we have determined that the primary temperature-dependent scattering mechanism affecting BEEM electron transport is acoustic phonon absorption in the Si substrate. Within the uncertainty of the measurements of  $\lambda_a$ , no energy dependence was observed at RT or 77 K. This result and the aforementioned relatively small temperature dependence of  $\lambda_a$  indicate that the mean free path for scattering from defects in the Au overlayer is significantly smaller than that for inelastic electron-electron scattering or for electron-phonon scattering. Evidence for reductions in the BEEM current for large surface gradients has been obtained for microscopy images taken with sufficiently sharp STM tips, and this has been correlated with the increase in path length to the interface, assuming that the probability of transmission is independent of the angle of incidence. This result provides strong evidence that electron transport through the Au overlayer is essentially ballistic and that the observed violation of transverse momentum conservation occurs at the interfacial region.

### *II.B. Hot-Electron Scattering Processes*

A schematic of BEEM electron transport across a M-S Schottky interface is shown in Fig. 6. Electrons injected into the metal overlayer from the STM tip will have an energy distribution which decays exponentially from a maximum value of  $eV_T$ . All electrons which approach the semiconducting region with an energy which is less than the Schottky barrier height,  $\Phi_S$ , will be scattered back into the metal. A fraction of the electrons which approach the semiconducting region with an energy greater than  $\Phi_S$  will travel across the barrier and be detected as a BEEM electron. The magnitude of the collected BEEM current is strongly influenced by scattering mechanisms in the metal overlayer, at the metallurgical interface, and within the semiconducting substrate.

A determination of the relative length scales of elastic and inelastic scattering processes in the metal overlayer is especially important since these scattering events have a direct effect on the resolution of BEEM at the M-S interface and limit the range of metal overlayer thicknesses which can be probed. Electrons can scatter elastically off defect sites or quasi-elastically by emission or absorption of acoustic phonons. For metals with more than one atom per primitive basis, the emission and absorption of optical phonons is also possible (Au has only one atom in its primitive basis). Although the energy quanta of acoustic phonons are typically on the order of

a few meV, the energy quanta of optical phonons can exceed 50 meV for compound metals. Therefore, the determination of whether electron scattering with optical phonons is considered to be a quasi-elastic process depends on the particular modes available for that system. Hot-electrons can also undergo inelastic electron-electron collisions with electrons near the Fermi level resulting in an average energy loss of half of their original kinetic energy. When the inelastic mean free path for scattering,  $\lambda_i$ , is of the same order as the elastic mean free path,  $\lambda_e$ , the transport process is essentially ballistic since electrons which have undergone multiple scattering events will, on average, not have enough kinetic energy to cross the Schottky barrier. In this limit, the BEEM current,  $I_b$ , should show a clear exponential dependence on metal film thickness with  $\lambda_a$  measured in a BEEM experiment given by  $1/\lambda_a = 1/\lambda_i + 1/\lambda_e$ . In the limit where  $\lambda_e \ll \lambda_i$ , the transport is expected to be diffusive in nature since the probability of undergoing multiple elastic scattering events before scattering inelastically is high. This will result in an electron momentum distribution at the M-S interface which is completely independent of the momentum distribution at the point of injection.

At the M-S interface, a fraction of the incident electrons will backscatter into the metal overlayer due to quantum mechanical reflection. For non-epitaxial systems and non-abrupt interfaces, there will be a break in symmetry parallel to the interface which will result in additional scattering at the interface. For epitaxial systems, the transverse momentum of the electron is expected to be conserved as it travels from the metal to the semiconductor. This condition will result in a critical angle for transport into the semiconductor substrate which increases as a function of the energy of the incident electron<sup>5</sup>. As a direct consequence of transverse momentum conservation, either a delayed or soft threshold for  $I_b$  is expected for electron transport into semiconductor surfaces where the projection of the conduction band minimum is not on the surface Brillouin zone center.

Within the semiconductor substrate, electrons can scatter by emission or absorption of either acoustic or optical phonons. As shown in Fig. 6, the position of the Schottky barrier maximum is not at the metallurgical M-S interface but is shifted by a few nanometers into the semiconductor due to the image potential. Electrons with energies just over the threshold for transmission that excite phonons in the region before the Schottky barrier maximum are expected to have a high probability of re-entering the metal. Beyond the Schottky barrier maximum, the internal electric field in the depletion region accelerates the electrons toward the interior of n-type semiconductors. Therefore, the effect of phonon scattering on the magnitude of  $I_b$  in the region beyond the Schottky barrier maximum depends on the doping density of the semiconductor since this defines the length of the depletion region, and thus the acceleration rate. For the 2-4 Ω-cm samples used in this experiment, the distance to the Schottky barrier maximum,  $d_{SBM}$ , and the depletion depth,  $d_{dep}$ , are calculated to be ~50 Å and ~1 μm, respectively<sup>14</sup>. Since this is a relatively low doping density, electrons which scatter in the region just beyond the Schottky barrier maximum are expected to have an equal probability of either re-entering the metal or passing through the semiconductor depletion region. Once the kinetic energy of the electrons in the semiconductor exceeds  $E_g$ , electron-hole pair generation, or impact ionization, becomes possible. Since the internal electric field in the semiconductor will sweep the electrons toward the interior of the semiconductor and the hole towards the metal, an electron multiplication process occurs<sup>15</sup>.

For metal overlayers more than a few monolayers thick,  $\Phi_s$ ,  $d_{dep}$ , and  $d_{SBM}$  are expected to be coverage independent. Assuming that quantum interference effects can be neglected, the BEEM current can then be expressed as a product of the transmissivities through the metal overlayer, across the metallurgical interface, and through the semiconductor depletion region. The proportion of electrons which traverse the metal region with energy,  $E$ , will decay exponentially with the path length to the metallurgical interface,  $d_m/\cos(\theta)$ , where  $\theta$  defines the injection angle from the surface normal. This results in the following expression for the measured BEEM current,

$$I_B(E, T, d_m) = I_{tip} A(E) B(E, T) \exp[-d_m / \lambda_a(E, T) \cos(\theta)], \quad (II.1)$$

where  $A(E)$  is a kinematic transmission factor for electron transport from the metal overlayer into the semiconductor lattice,  $B(E, T)$  is the transmission factor for electron transport through the semiconductor depletion region, and  $I_{tip}$  is the injected current into the metal overlayer. The factor  $A(E)$  is assumed to be independent of the angle of incidence, which results from the assumption of non-conservation of transverse momentum at the interface<sup>6</sup>. Both  $B(E, T)$  and  $\lambda_a(E, T)$  should be temperature-dependent since the path length for phonon absorption will depend strongly on the phonon populations in the metal and semiconductor regions.

### *IIC. Experimental*

The BEEM measurements were performed with a modified Kaiser-Jaklevic STM design<sup>16</sup> which has three, separate, orthogonal, planar piezo drives for tip control and uses a stepper motor for the fine approach of the sample. The STM is housed in a liquid nitrogen ( $LN_2$ ) dewar which is incorporated into a glove box. To perform low temperature BEEM, the dewar is purged with high-purity  $N_2$  before backfilling with  $LN_2$ . Although the original design of the STM placed the tip current amplifier and BEEM current amplifier in the dewar near the STM head to reduce pickup noise, significant changes in the performance characteristics of the operational amplifiers and the feedback resistors were observed when immersed in  $LN_2$ . Since maintaining an amplifier gain which is independent of the temperature of the sample is crucial to measuring the temperature dependence of the BEEM transmissivity, the amplifiers were moved outside of the dewar into separate die-cast aluminum boxes which are attached to the STM support flange via standard BNC connectors. Low temperature compatible ultra-thin coax<sup>17</sup> is used to carry the signals to the amplifiers with the outer conductor biased at the same potential as the inner conductor to reduce capacitive coupling. The outer insulating sheath of the coax was also removed to improve the flexibility of the coax at low temperatures.

The Au/Si(100) Schottky diodes were prepared from n-type 2-4  $\Omega\text{-cm}$  Si. An Ohmic contact was applied to the back of each sample by melting indium onto an area of the sample which had been roughened with a diamond scribe. The quality of the Ohmic contacts made by this method were checked by measuring the resistance across Si samples with indium applied to both the front and back of the sample. Resistance values across these In-Si-In junctions of  $\sim 40 \Omega$  at RT were consistently measured. The oxide of the Si was removed by dipping the samples in a solution of 10:1 ethanol:HF solution for 1-2 minutes. After removal from the etching solution, the samples were dried with high-purity  $N_2$  before insertion into a cryopumped evaporation unit.

The Au was evaporated from a tungsten thermal boat source through a shadow mask to form a rectangular 2.5 mm x 10 mm diode. The nominal deposition rate was ~0.5 Å/s and was monitored with a quartz crystal microbalance. The base pressure of the evaporation unit is ~10<sup>-8</sup> Torr with a typical evaporation pressure of ~5 x 10<sup>-7</sup> Torr. Calibration of the Au overlayer coverages measured with the quartz crystal microbalance was performed periodically using Rutherford backscattering at a separate facility. The uncertainty in the measurement of the Au overlayer thickness is estimated to be within ±5%. It is also noted that in the early stages of this study, samples were prepared by applying the indium contact after the deposition of the Au to prevent any effect that solvation of indium in the etching solution might have on the etching procedure. However, this technique often resulted in images with large changes in the BEEM current which could not be correlated to any topographic features. It is assumed that this effect results from interdiffusion of Au and Si during the application of the indium since a previous Auger electron spectroscopy (AES)/low energy electron diffraction (LEED) study<sup>18</sup> and a transmission electron microscopy (TEM) study<sup>19</sup> have provided evidence for gold silicide formation at the M-S interface at temperatures well below the eutectic of 363 °C.

Both Au and Pt-Ir (90:10) STM tips were chosen for the BEEM measurements since they do not form a native oxide under ambient conditions. The Au tips were prepared from 0.25 mm diameter wire either by DC electrochemical etching in a 50:50 HCl:ethanol solution or by cleaving at a very sharp angle with a razor blade. Etching produced very sharp whisker-like tips, as examined under an optical microscope. However, instabilities in the tunnel current during the fine sample approach were often observed for etched tips which was correlated to the poor mechanical rigidity of the whisker-like tip structures. Since cleaved tips did not exhibit instabilities during the fine approach, this was the primary method used for making Au tips. The STM images from both etched and cleaved Au tips showed similar topographies. The Pt-Ir tips were prepared from 0.50 mm diameter wire by cutting the wire at a very sharp angle with ordinary wire snippers. Since previous STM studies with Au tips have shown that Au atoms field desorb at a relatively low tip bias of -3.2 V<sup>20</sup>, the energy range for our spectroscopic data was limited to 1.2 eV to stay well below the field desorption limit.

## IID. RESULTS

### IID.1 Temperature-dependent BEEM spectroscopy

BEEM spectroscopy spectra were obtained at both RT and 77 K over a range of Au overlayer thicknesses from ~65 Å to ~340 Å. A semilog plot of the percent transmittance ( $I_B/I_T \times 100$ ) as a function of Au overlayer thickness at a tip bias of -1.2 V is shown in Fig. 7. A minimum of 80 spectra were collected over a surface area of ~2000 Å x ~2000 Å for each coverage and temperature. A histogram of the transmittances was plotted for each data set, and the value of the average transmittance was derived by fitting a Gaussian curve to each histogram with the error bars representing the full-width at half-maximum of the curve. For coverages with both a 77 K and RT transmittance, both data sets were collected from the same sample within 6 hours of each other (the RT data was collected first). The linear curves through the data sets represent least-squares fits applied to the data. Since averaging over such large data sets should eliminate any effects of surface gradient on the transmissivity,  $\lambda_a$  can be obtained from the inverse of the slope

of the least squares fit. The zero length transmittance,  $I_o(E,T) = A(E)B(E,T)$ , is obtained from the intercept.

The absolute value of  $A(E)$  and  $B(E,T)$  can not be determined independently from our measurements. However, the temperature dependence of  $B(E,T)$  can be determined by calculating the ratio of the zero length transmittances at 77 K and RT,  $I_o(E,77K)/I_o(E,RT) = B(E,77K)/B(E,RT)$ , since  $A(E)$  is expected to be independent of temperature. A 50 meV increase in  $\Phi_S$  is measured at 77 K due to the increase in  $E_g$  of Si at low temperatures; therefore, the ratio  $I_o(E,77K)/I_o(E,RT)$  is calculated for constant kinetic energy in the Si conduction band and is plotted in Fig. 8a. A value of  $1.79 \pm 0.09$  over a kinetic energy range of 140 meV to 380 meV is obtained which indicates that approximately half of the electrons which cross into the depletion region at RT back scatter into the metal overlayer after phonon absorption.

A plot of  $\lambda_a$  as a function of tip bias at both RT and 77 K is shown in Fig. 8b. With our instrumentation,  $\lambda_a$  could be measured accurately down to energies of  $\sim$ 100 meV above  $\Phi_S$  over the range of Au thicknesses measured in this study. A value of  $133 \pm 2$  Å and  $147 \pm 6$  Å were measured for  $\lambda_a$  at RT and 77 K, respectively. As can be seen in Fig. 8b, no energy dependence for  $\lambda_a$  at either temperature is observed within the uncertainty of the measurements. The value of  $133 \pm 2$  Å that we measure for  $\lambda_a$  at RT deviates slightly from the previously measured values<sup>21,22</sup> of 125 Å and 140 Å for Au/Si BEEM measurements. This deviation most likely results from our measurement of  $\lambda_a$  over a larger range of sample thicknesses than in the earlier studies. However, differences in the sample preparation procedure and in the uncertainties of the metal overlayer thicknesses may also account for these slight discrepancies. In contrast to these results, an attenuation length of  $\lambda_a = 30$  Å for the system Au/GaP(110) was derived from Monte Carlo simulations of BEEM data<sup>12</sup>. This low value for  $\lambda_a$  is probably an effect of the different growth morphology of Au on GaP(110) over the range of thicknesses measured in their study.

## IID.2 Room temperature BEEM imaging

Although our spectroscopy data, which measured only an 11% increase in  $\lambda_a$  at 77 K, indicate that quasi-elastic scattering from acoustic phonons in the Au overlayer has a negligible effect on the temperature-dependent transmission probability, this does not preclude the possibility that elastic scattering will affect the trajectory of electrons in the metal overlayer. Therefore, a detailed BEEM microscopy analysis of several Au/Si(100) samples was performed with both Au and Pt-Ir STM tips in an attempt to correlate surface topographic features with changes in the BEEM current. Since electron injection over a surface topographic feature with a non-zero gradient will increase the path length to the M-S interface, it is expected that reductions in the BEEM current should be observed at large surface gradients. This effect is often called the “search-light effect.” A calculation of the expected reduction in the BEEM current as a function of injection angle is shown in Fig. 9. This calculation assumes that the probability of transmission across the Schottky barrier is independent of the angle of incidence, *i.e.* transverse momentum is not conserved at the interface. For thin Au overlayers, a very large surface gradient is needed to observe appreciable decreases in  $I_B$  (for a 50 Å overlayer, a gradient of  $\sim$ 70° is needed to observe a 50% reduction in  $I_B$ ). At larger Au overlayer thicknesses,  $I_B$  is more

sensitive to surface gradient (for a 300 Å overlayer, a gradient of ~40°. is needed to observe a 50% reduction in  $I_B$ ), but the magnitude of  $I_B$  is near the limit of detection.

From analysis of our BEEM data measured with Au tips and Pt-Ir tips, it was determined that the tip apex geometry is the primary factor that influences the spatial resolution of BEEM. For imaging with Au tips, changes in the tip geometry were often observed during STM scans and often resulted in featureless images which we correlate to an extremely blunt tip apex. Imaging with Pt-Ir tips produced much more consistent STM topographies. A schematic of the effect that tip apex geometry has on the resolved surface topography and on the injection angle of the electrons is shown in Fig. 10 where the dashed lines represent the resolved topographies for each tip condition. For the range of Au overlayer thickness in this study, rounded surface features with a spatial extent of ~50 Å to ~200 Å and heights from ~30 Å to ~80 Å were observed. Since surface gradients large enough to observe appreciable changes in the BEEM current exist only near the bottom of the crevices between these rounded structures, a sharp tip protrusion which is longer than the average height of the rounded surface structures is needed to probe these regions as shown in Fig. 10b. A BEEM image of a ~500 Å x ~500 Å area of a 103 Å Au/Si(100) sample imaged with a Pt-Ir tip is shown in Fig. 11. Asymmetric surface features are observed in the STM topography shown in Fig. 11a with surface gradients as large as ~75° being measured. The corresponding BEEM image shown in Fig. 11b shows regions of reduced BEEM current of up to ~85% which correlate with the regions of the STM topography where high surface gradients were measured. During collection of the data, the reductions in the BEEM current were observed for both scan directions which indicates that this effect does not result from the tracking of the feedback control system. Images performed below the Schottky barrier height were also featureless which precludes the possibility that the features observed are due to a coupling of the BEEM current with the signals from the piezoelectric drives.

## *II.E. Discussion*

The exponential nature of the transmissivity plots at both 77 K and RT shown in Fig. 7 gives strong evidence that the attenuation length model, Eqn. II.1, is valid for Au overlayers over the range of ~65 Å to ~340 Å. The observation that the attenuation length in the metal and the transmissivity through the semiconductor depletion region are temperature-dependent is expected since the phonon populations in both regions should decrease as a function of temperature. To estimate the relative interaction lengths of both elastic and inelastic scattering events in the metal overlayer, both the temperature and the energy dependence of  $\lambda_a$  must be taken into account. Assuming that the contribution of multiply scattered electrons to the BEEM current can be neglected, the attenuation length of the BEEM electrons in the metal overlayer can be expressed as  $1/\lambda_a = 1/\lambda_i + 1/\lambda_{ph} + 1/\lambda_d$  where  $\lambda_i$  is the path length for inelastic electron-electron scattering,  $\lambda_{ph}$  is the path length for acoustic phonon scattering, and  $\lambda_d$  is the path length for defect scattering. Since sharply reduced BEEM currents at regions of large gradients in the surface topography have been observed, this strongly suggests that this approximation is valid. The probability for inelastic electron-electron scattering is theoretically predicted to have a  $(E + E_F)/E^2$  dependence where  $E_F$  is the Fermi energy of the metal<sup>23</sup>. This should result in a decrease in  $\lambda_i$  of ~40% over the energy range 0.9 eV to 1.2 eV. Therefore, the lack of energy dependence for  $\lambda_a$  indicates that the path length for elastic scattering events is considerably smaller than that

for electron-electron scattering. The value of  $\lambda_{ph}$  is expected<sup>24</sup> to be approximately equal to the conductivity mean free path of pure bulk Au which is 417 Å at 273 K and 1668 Å at 77 K. Since the measured value of  $\lambda_a$  is only 133 Å at RT and a relatively small 11% increase in this value is measured at 77 K, this indicates that the scattering in the metal overlayer is primarily dominated by elastic scattering from defect sites.

One might be tempted to conclude that the measurement of a smaller value for  $\lambda_e$  than  $\lambda_i$  should result in diffuse transport through the metal overlayer. However, the actual magnitude of  $\lambda_e$  which is required for transition to the diffuse transport regime is difficult to determine from first principles<sup>14</sup>. Our experimental observation of the “search-light effect,” as well as previously published BEEM results for Au/Si interfaces<sup>8,21</sup> which have measured nanometer resolution at the M-S interface for similar Au overlayer thicknesses, indicate that the electron transport is ballistic. In other words, once an electron is deflected from its original trajectory by an elastic scattering event, the probability of it eventually crossing the M-S interface without undergoing an inelastic scatter is still quite low for the defect density of these films.

Since RT grown Au/Si(100) is a non-epitaxial system with a very large lattice mismatch (~25%), it is expected that the metal overlayer will have a very large defect density during the first several layers of growth. In fact, a previous AES/LEED study<sup>18</sup> of Au/Si interface growth at RT has indicated that gold silicide is present in the overlayer and that no long range order is observed with LEED for coverages up to ~100 Å. Beyond this coverage, no gold silicide was detected and diffuse ring structures which transformed to distinct multi-domain (111) LEED spots by a coverage of ~300 Å were observed. This growth morphology may also partially explain the large discrepancy of the value of  $\lambda_a$  measured by BEEM and by internal photoemission since the Au film thicknesses measured in the internal photoemission studies were considerably larger than those measured in this study. In fact, Ludeke and Bauer<sup>11</sup> have come to a similar conclusion for the large discrepancy between the value of  $\lambda_a$  that they measure for Pd/Si with BEEM (31 Å at 1 eV) and the value measured<sup>2</sup> by internal photoemission (170 Å at 0.85 eV). For epitaxial systems where the metal overlayer defect density can be more carefully controlled, there should be better agreement between the attenuation lengths measured by BEEM and internal photoemission. Attenuation length measurements at 77 K for the *epitaxial* CoSi<sub>2</sub>/Si(111) interface have resulted in values of  $\lambda_a = 70$  Å by BEEM spectroscopy<sup>25</sup> and  $\lambda_a = 90$  Å by internal photoemission<sup>26</sup> at an energy of 0.8 eV which gives credence to this model.

The measurement of almost twice the transmissivity through the depletion region of the Si at 77 K is in direct contradiction with previous analytical calculations<sup>27,28</sup> which predicted only an ~15% increase in the transmissivity for Au/Si at 77 K. Both studies modeled the temperature-dependent collection efficiency in the depletion region as due to electron interactions with the 63 meV transverse optical phonons in Si. However, all semiconductors with the diamond structure have a low frequency transverse acoustic phonon branch which has an anomalously flat dispersion away from the zone center that results from the strong coupling of the lattice ions with the electronic states in the semiconductor<sup>29</sup>. It is expected that electrons over the energy range measured in this study should have a significant probability for interaction with these thermally excited transverse acoustic phonons<sup>30</sup>. In addition, the transverse acoustic phonon energy<sup>31</sup> of ~20 meV for Si is small enough to expect a significant population of this mode at RT. Since the models used in the previously mentioned analytical calculations only considered electron scattering with optical phonons, the neglecting of acoustic phonon scattering modes is the most probable origin of the large discrepancy. This large coupling of the electrons to the acoustic

phonon modes may also partially account for the similarities of BEEM spectroscopy data for both the Si(100) and Si(111) surfaces since phonon scattering events before the Schottky barrier maximum would provide an additional source of transverse momentum. However, the relative importance of this effect, when compared to scattering at the interface which results from the non-epitaxial nature of the Au/Si system, can not be determined at this time since temperature-dependent BEEM measurements on the Au/Si(111) have not been performed.

The observation of nearly featureless BEEM images of Au/Si(100) by several groups is most certainly an effect of tip apex geometry. Although we have obtained images which show clear evidence for the search-light effect, the great majority of images taken with both Au and Pt-Ir tips also do not show this effect. In addition, the lifetime of the tips with an apex that allows imaging of the "search-light effect" are typically limited to a fraction of a BEEM scan (a typical BEEM scan takes ~15 min. for our microscope). This is presumably due to the delicate nature of such a sharp protrusion. Since the yield strength of Pt-Ir is approximately twice that of Au, the superior mechanical stability of Pt-Ir tips during imaging is not unexpected. Although, the quality of Au tips for imaging was found to be inferior to Pt-Ir tips, the contrary was true for spectroscopy. Tip contamination problems were not encountered very often for either Au or Pt-Ir tips at RT; however, large instabilities in the tunneling current were often observed when using Pt-Ir tips at 77 K. Therefore, all of the spectroscopy data reported in this paper were taken using Au STM tips.

Although the tip apex geometry is found to play a major role in the observed BEEM topography, sample preparation procedure might also explain some of the discrepancies observed for different groups studying Au/Si interfaces. Ideally, preparing samples under UHV conditions should provide the most controlled, contamination free interfaces. However, great care must be taken to ensure that the Au source is properly outgased before deposition since Si is a very reactive surface. For Si samples prepared by a wet chemical etch before Au deposition, contamination problems during deposition are reduced since the Si surface is left with a hydrogen passivation layer<sup>32</sup>. On the other hand, contamination problems can occur during the etching process itself if the composition of the etching solution is not carefully controlled. Since PES studies have indicated that a gold silicide surface segregation layer exists during the initial stages of overlayer growth<sup>10,33</sup>, it is expected that this silicide layer would have an adverse effect on BEEM imaging performed in air due to the formation of an insulating SiO<sub>2</sub> overlayer. No indication of this effect has been observed for the samples prepared in this study which either indicates that the silicide is effectively buried for the range of sample thicknesses measured in this study or that the hydrogen passivation layer prevents the formation of the silicide layer.

#### *IIF. Conclusions*

The lack of energy dependence and the relatively small temperature-dependent change in  $\lambda_a$  that has been measured with BEEM are consistent with the dominance of electron scattering from defects over the range of Au overlayers measured in this study. In addition, the large discrepancy between the values of  $\lambda_a$  measured by BEEM and internal photoemission for Au/Si samples has been primarily attributed to the different growth morphology of Au at the higher coverages measured in the internal photoemission studies. Our transport measurements, which have determined that almost half of the electrons which pass into the Si depletion region are scattered back into the metal region at RT due to phonon absorption, indicate that previously

published analytical calculations<sup>27,28</sup> have underestimated the importance of hot-electron interactions with the acoustic phonon modes in the Si.

The measurement of the “search-light effect” for Au/Si(100) gives strong evidence that BEEM electron transport through the metal overlayer is essentially ballistic, *i.e.* the trajectory of the injected electrons through the Au overlayer remains unchanged, at energies up to 1.2 eV and for overlayer thicknesses up to a few hundred Angstroms. The observation of featureless BEEM images by previous groups has been attributed to the need of an extremely sharp tip apex to see this effect. The good agreement between the experimentally observed and the calculated reductions in the BEEM current using a model which assumes the transmission is independent of incident angle indicates that violation of transverse momentum conservation results from scattering at the metallurgical interface.

## References for Section II

- [1] C. R. Crowell and S. M. Sze, in *Physics of Thin Films*, edited by G. Hass and R. F. Thun (Academic, New York, 1967), Vol. 4, p. 325.
- [2] C. R. Crowell, W. G. Spitzer, L. E. Howarth, and E. E. LaBate, Phys. Rev. **127**, 2006 (1962).
- [3] S. M. Sze, J. L. Molll, and T. Sugano, Solid-State Electron. **7**, 509 (1964).
- [4] R. W. Soshea and R. C. Lucas, Phys. Rev. **138**, A1182 (1965).
- [5] L. D. Bell and W. J. Kaiser, Phys. Rev. Lett. **61**, 2368 (1988).
- [6] L. J. Schowalter and E. Y. Lee, Phys. Rev. B **43**, 9308 (1991).
- [7] E. Y. Lee, B. R. Turner, L. J. Schowalter, and J. R. Jimenez, J. Vac. Sci. Technol. B **11**, 1579 (1993).
- [8] H. Palm, M. Arbes, and M. Schulz, Phys. Rev. Lett. **71**, 2224 (1993).
- [9] A. Fernandez, H. D. Hallen, T. Huang, R. A. Buhrman, and J. Silcox, Appl. Phys. Lett. **69**, 2679 (1990).
- [10] M. T. Cuberes, A. Bauer, H. J. Wen, D. Vandré, M. Prietsch, and G. Kaindl, J. Vac. Sci. Technol. B **12**, 2422 (1994).
- [11] R. Ludeke and A. Bauer, Phys. Rev. Lett. **71**, 1760 (1993).
- [12] A. Bauer, M. T. Cuberes, M. Prietsch, and G. Kaindl, Phys. Rev. Lett. **71**, 149 (1993).
- [13] M. Prietsch and R. Ludeke, Phys. Rev. Lett. **66**, 2511 (1991).
- [14] E. Y. Lee, Ph. D. dissertation, Rensselaer Polytechnic Institute, 1992 (unpublished).
- [15] A. Bauer and R. Ludeke, Phys. Rev. Lett. **72**, 928 (1994).
- [16] W. J. Kaiser and R. C. Jaklevic, Surf. Sci. **181**, **55** (1987).
- [17] Lake Shore Cryotronics, C-1 coax cable, part number 9002-002-025.
- [18] K. Oura and T. Hanawa, Surf. Sci. **82**, 202 (1979).
- [19] P.-H. Chang, G. Berman, and C. C. Chen, J. Appl. Phys. **63**, 1473 (1988).
- [20] H. J. Mamin, P. H. Guethner, and D. Rugar, Phys. Rev. Lett. **65**, 2418 (1990).
- [21] A. M. Milliken, S. J. Manion, W. J. Kaiser, L. D. Bell, and M. H. Heckt, Phys. Rev. B **46**, 12826 (1992).
- [22] H. Palm, M. Arbes, and M. Schulz, Appl. Phys. A **56**, 1 (1993).
- [23] J. J. Quin, Phys. Rev. **126**, 1453 (1962).
- [24] N. W. Ashcroft and N. D. Mermin, *Solid State Physics* (W. B. Saunders Company, Philadelphia, 1976).

- [25] E. Y. Lee, H. Sirringhaus, and H. von Känel, *Surf. Sci.* **314**, L823 (1994).
- [26] J. Y. Duboz and P. A. Badoz, *Phys. Rev. B* **44**, 8061 (1991).
- [27] C. R. Crowell and S. M. Sze, *Solid-State Electron.* **8**, 979 (1965).
- [28] E. Y. Lee and L. J. Schowalter, *J. Appl. Phys.* **70**, 2156 (1991).
- [29] W. Weber, *Phys. Rev. Lett.* **33**, 371 (1974).
- [30] E. J. Melé (private communication).
- [31] H. Palevsky, D. J. Hughes, W. Kley, and E. Tunkelo, *Phys. Rev. Lett.* **2**, 258 (1959).
- [32] H. Ubara, T. Imura, and A. Hiraki, *Solid State Commun.* **50**, 673 (1984).
- [33] J.-J. Yeh, J. Hwang, K. Bertness, D. J. Friedman, R. Cao, , and I. Lindau, *Phys. Rev. Lett.* **70**, 3768 (1993).

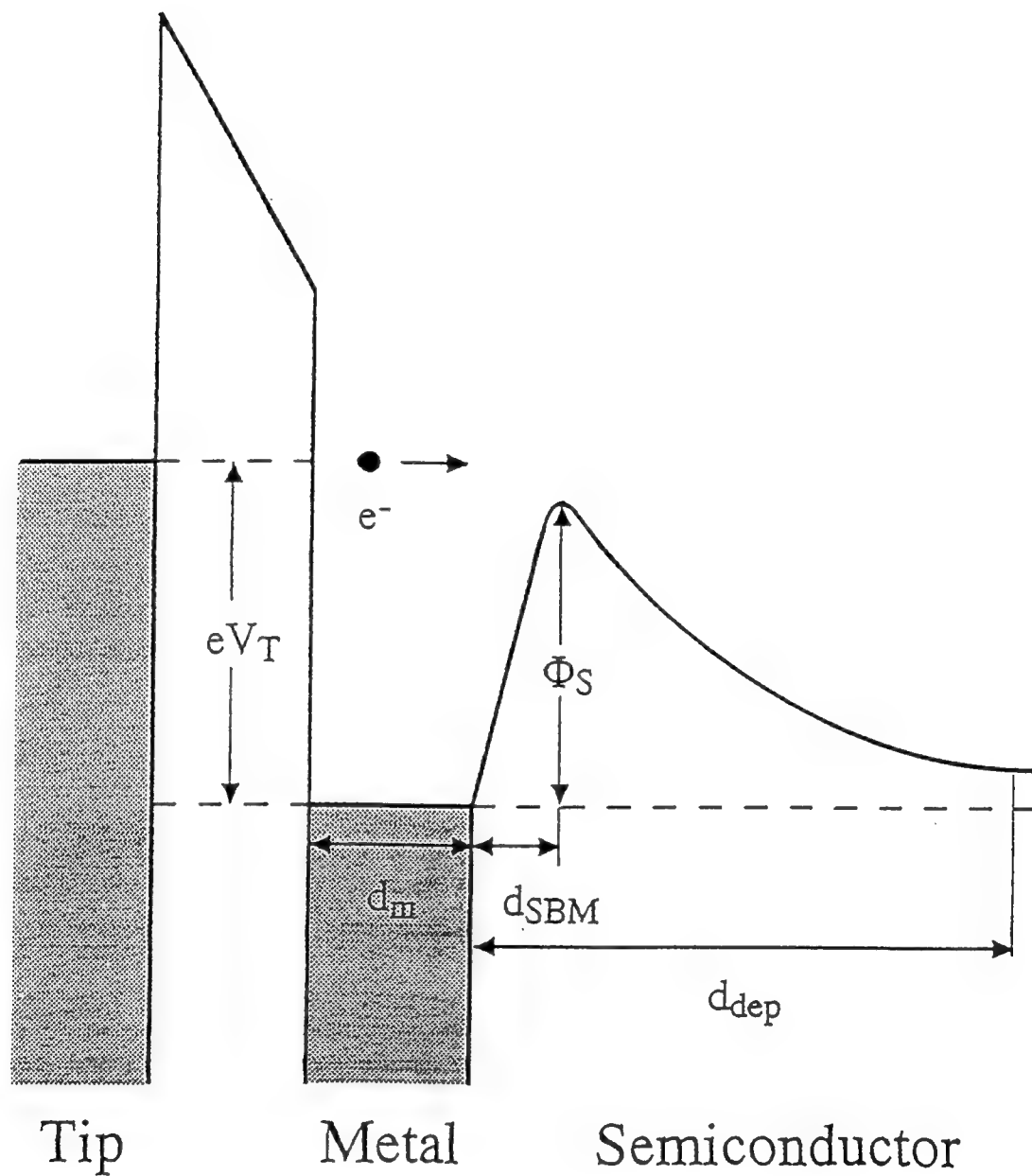


*Figure 6:* Schematic of BEEM electron transport across a metal-semiconductor Schottky interface (not drawn to scale). For electrons injected into the metal overlayer with a tip bias greater than the Schottky barrier,  $\Phi_S$ , a fraction of the injected electrons will travel across the barrier and be detected as a BEEM electron. The magnitude of the BEEM current is strongly influenced by scattering processes in the metal overlayer, at the metallurgical interface, and within the semiconducting substrate.

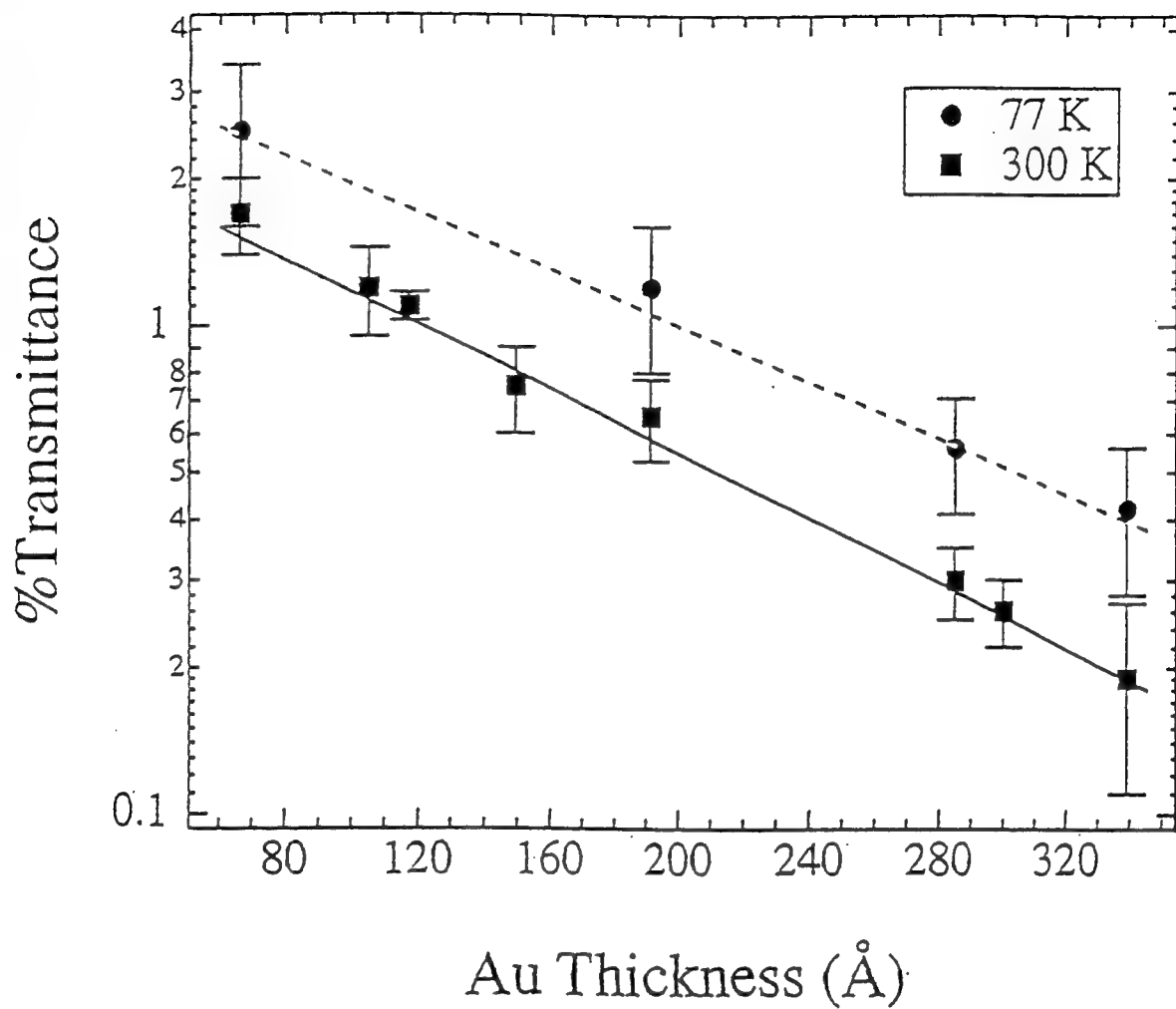


*Figure 7:* Semilog plot of BEEM transmittances,  $I_B/I_T \times 100$ , at a tip bias of -1.2 V measured on several Au/Si(100) samples at 77 K (circles) and RT (squares). A minimum of 80 spectra were collected at each coverage and temperature. The linear curves through the data sets represent least-squares fits applied to the data. From the slope and intercept of these curves, the attenuation length of the electrons in the Au overlayer,  $\lambda_a$ , and the zero thickness transmittance,  $I_0$ , are determined.

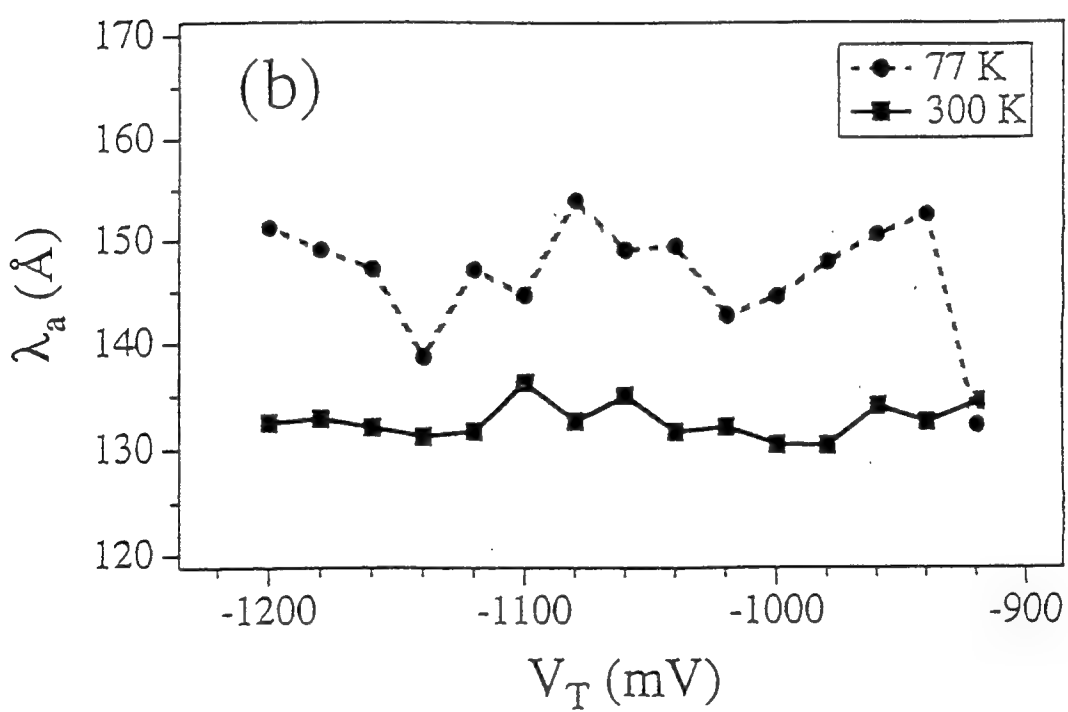
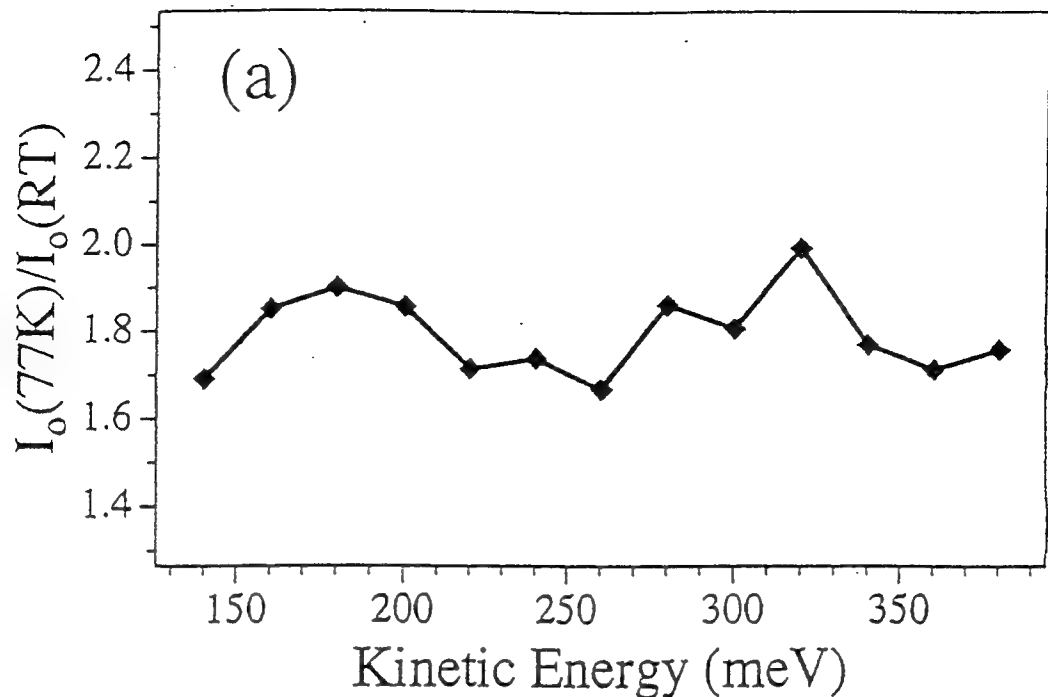
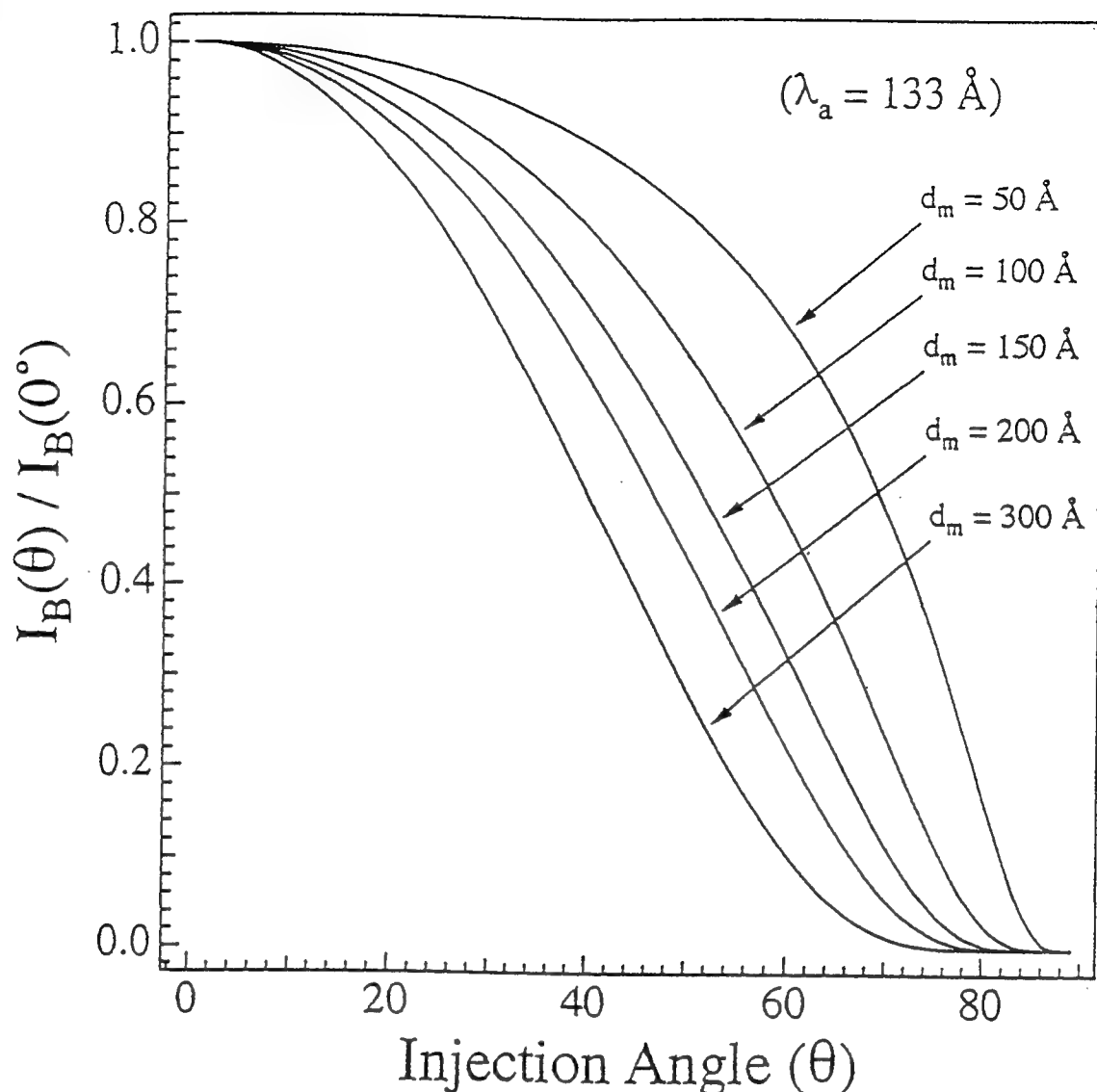


Figure 8: (a) Plot of the ratio of the zero thickness transmittance at 77 K to that at RT,  $I_o(77\text{K})/I_o(\text{RT})$ , as a function of kinetic energy,  $eV_T - \Phi_S$ , in the semiconductor. An average value of  $1.79 \pm 0.09$  over the kinetic energy range of 140 meV to 380 meV is obtained for  $I_o(77\text{K})/I_o(\text{RT})$ . (b) Plot of the attenuation length of the BEEM electrons in the Au overlayer at both 77 K (circles) and RT (squares) as a function of tip bias. Only a slight temperature dependence to  $\lambda_a$  is observed,  $\lambda_a(300\text{K}) = 133 \pm 2$  Å and  $\lambda_a(77\text{K}) = 147 \pm 6$  Å. Within the experimental uncertainty of these measurements, no energy dependence of  $\lambda_a$  is observed.



*Figure 9:* Calculation of the reduction of normalized BEEM current,  $I_B(\theta)/I_B(0^\circ)$ , that results from the increase in path length to the M-S interface for non-zero injection angles for several metal overlayer thicknesses. This calculation assumes that any electron reaching the M-S interface is equally likely to cross it regardless of its momentum parallel to the interface.

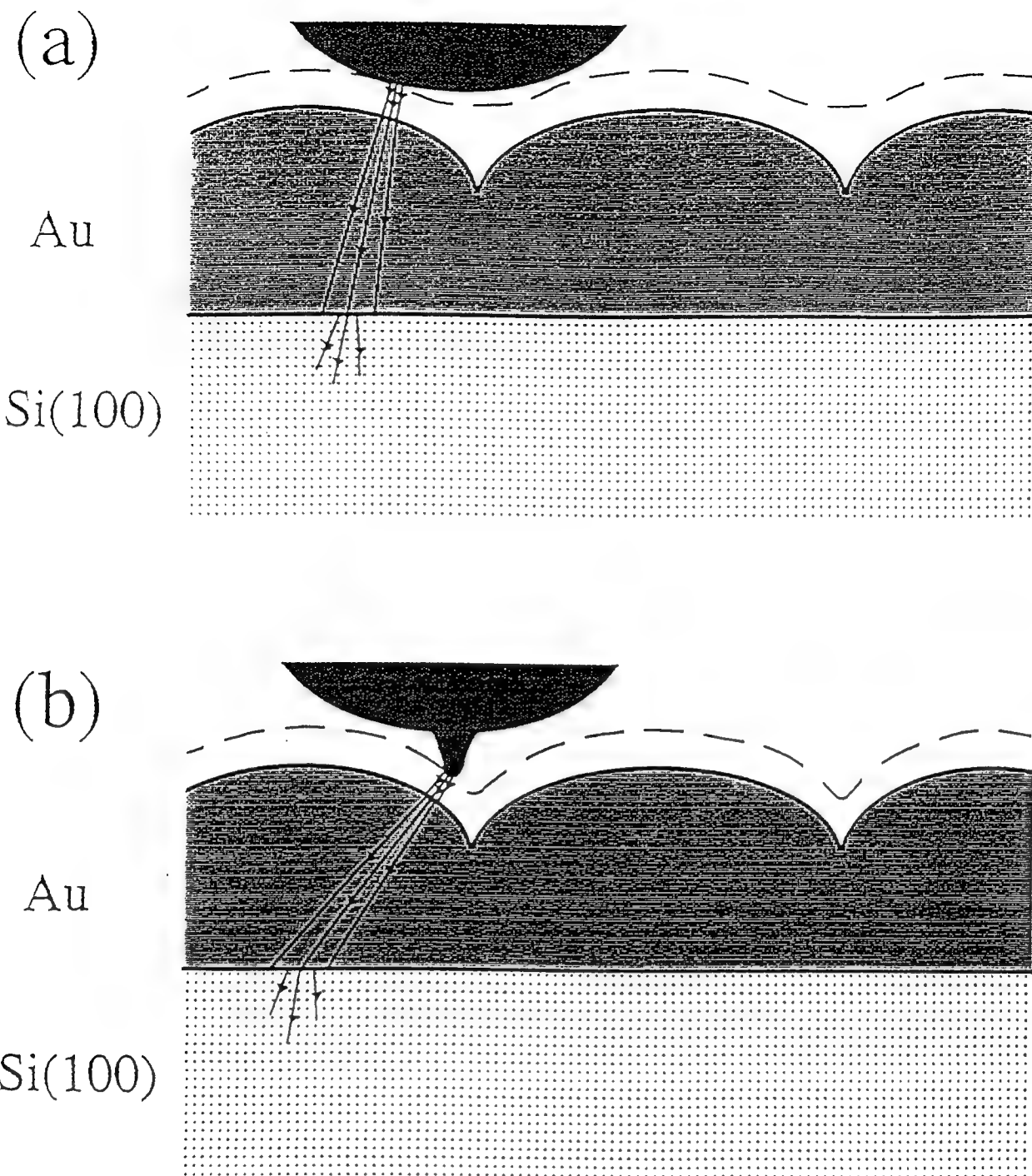


Figure 10: Schematic of the effect of tip apex geometry on the resolved topography (dashed lines) of the STM and the injection angle of the electrons. (a) Imaging with a tip apex which has a radius of curvature larger than the actual topographic features of the surface will result in an inability to resolve the surface regions with large gradients, *e.g.* the crevices between the rounded surface structures. (b) Imaging with a tip which has a sharp “mini tip” which is longer than the average corrugation height of the surface will result in a measured topography which closely mimics the actual topography.

11A



11B



Figure 11: (a) STM topographic image of a  $\sim 500 \text{ \AA} \times \sim 500 \text{ \AA}$  area of a  $103 \text{ \AA}$  Au/Si(100) sample ( $V_T = -1.2 \text{ V}$  and  $I_T = 5 \text{ nA}$ ). (b) BEEM image taken simultaneously with the topographic image shown in (a). The grey scale range for the BEEM image is 0-120 pA with dark areas representing low BEEM current. The grey scale range for the STM image is  $120 \text{ \AA}$  with light areas representing high surface features. Surface gradients as high as  $\sim 75^\circ$  are observed in the STM image and correlate to regions of the BEEM image with an  $\sim 85\%$  reduction in the BEEM current.

### **III. Design and installation of a scanning tunneling microscope for *in-situ* topographic and spectroscopic/BEEM measurements within our molecular beam epitaxy machine**

A scanning tunneling microscope that performs scanning tunneling microscopy, scanning tunneling spectroscopy, and ballistic electron emission microscopy measurements on 2-inch wafers has been designed and constructed. This instrument was constructed so that we could make BEEM measurements on reactive metal surfaces such a Pt or PtSi. Prior to constructing this instrument, we had tried passivating the PtSi surface by putting down a protective Au layer. However, the Au layer (particularly, the Au/PtSi interface) sufficiently complicated the interpretation of the BEEM measurements that we found this scheme unattractive. The *in-situ* instrument is incorporated into the Si preparation chamber of our cryo-pumped Fisons V90H Si/III-V molecular beam epitaxy machine. Its design uses two commercial<sup>1</sup> Burleigh inchworms: one for performing scanning tunneling microscopy measurements and a second for making a front contact which is necessary for the ballistic electron emission microscopy measurements. A schematic view of the microscope is shown in Fig. 12. The substrate holder for the V90H system is designed to handle wafers up to 6 inches in diameter. Therefore, a custom 6 inch diameter holder has been constructed which supports two 2-inch holders: one for performing reflection high energy electron diffraction measurements and a second which allows transfer of the wafer to the scanning tunneling microscope and also incorporates a removable shadow mask for growing metal/semiconductor Schottky diodes. Although the chamber vibrations generated by the cryopump and its compressor are quite severe, atomic-resolution images have been obtained with all of the system's pumps in operation as shown in Fig. 13. The enhanced stability of our design is attributed to our unique support system of the inchworm and wafer which are both manufactured from machinable ceramic, the use of Be-Cu springs with an extension length of 16 inches for vibration isolation, and the use of silicone O-rings for vibration damping.

This instrument was designed and constructed using ONR support. However, we initiated work on PtSi/Si and on Pt/ CaF<sub>2</sub> /Si. In Fig. 14, a BEEM spectrum obtained for PtSi/Si(111) is shown. A current onset at ~0.9 V is observed in the spectrum which corresponds to the previously published Schottky barrier heights measured for this system.<sup>2</sup> As mentioned in Section I, we are interested in using very thin layers of CaF<sub>2</sub> as resonant tunnel barriers. The *in-situ* STM/BEEM has allowed us to start exploring the local electrical and morphological aspects of this system.<sup>3</sup> In Fig. 15, an averaged BEEM spectrum is shown of a 10 nm Pt layer deposited on a 0.6 nm layer of CaF<sub>2</sub> on Si(111) n-type substrate. The most interesting aspect of this spectrum is the apparent resonant tunneling observed through the Pt/ CaF<sub>2</sub> layers at -1.8 V. The current maximum at about -4 V is due to direct injection into the CaF<sub>2</sub> conduction band.

#### **References for Section III**

- [1] Burleigh Instruments, Inc., ARIS-10 SPM approach module.
- [2] E. Y. Lee, B. R. Turner, L. J. Schowalter, and J. R. Jimenez, J. Vac. Sci. Technol. B11, 1580 (1993).
- [3] C. A. Ventrice, Jr., V. P. LaBella, B. Gallo, and L. J. Schowalter (in preparation).

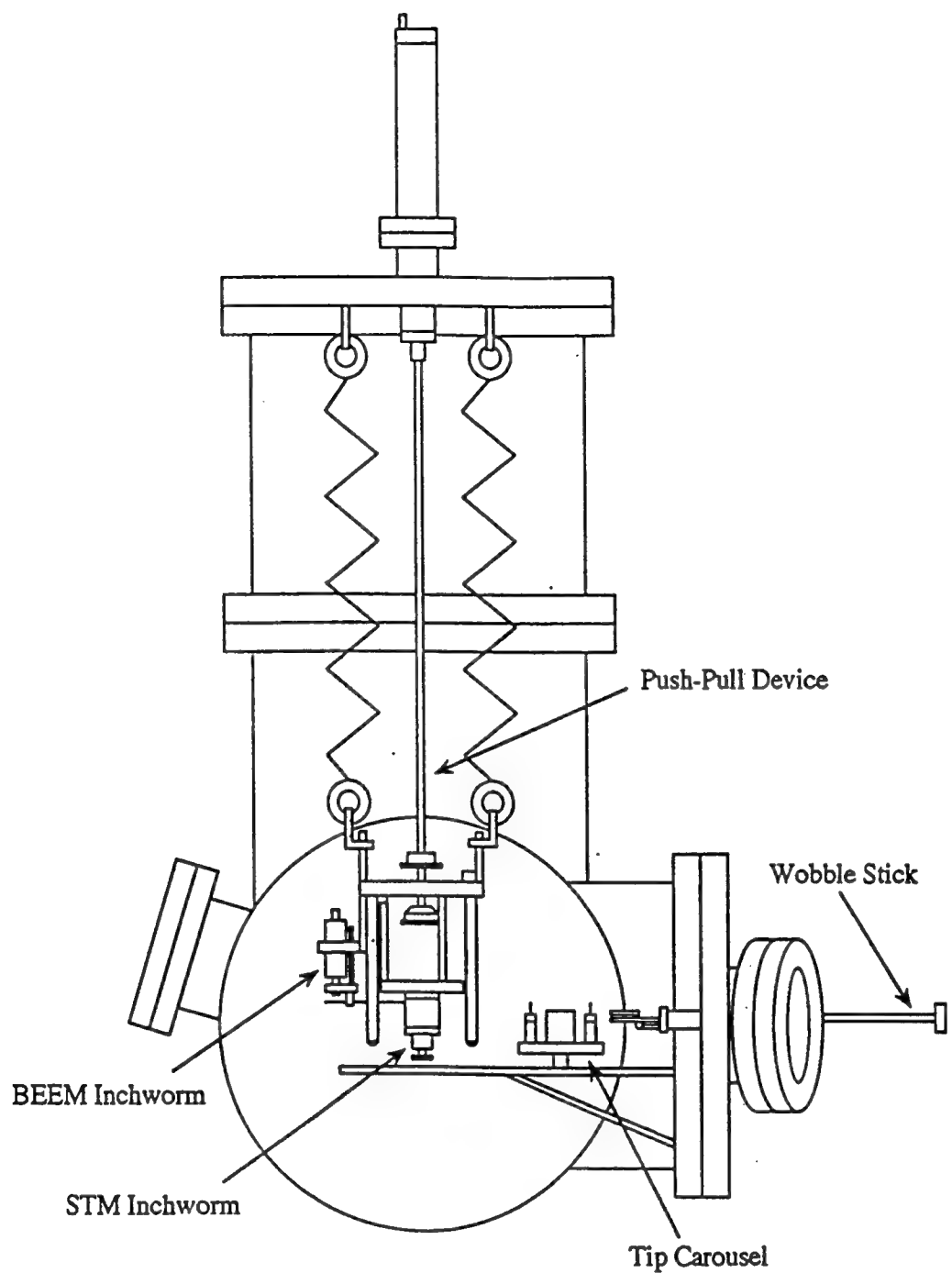


*Figure 12:* Schematic of the side view of the preparation chamber of the V90H MBE machine with the wafer-STM installed. The STM design uses two Burleigh inchworms: one which has a scanner tube for STM measurements and a second with an electrode which is used to make a front contact for BEEM measurements. The STM incorporates a push-pull device to allow the transfer of wafers through the preparation chamber to the deposition chamber. The diameter of the preparation chamber is 15 inches and the distance from the STM support flange to the preparation chamber center line is 25 inches.

### STM: Si/Si(111)

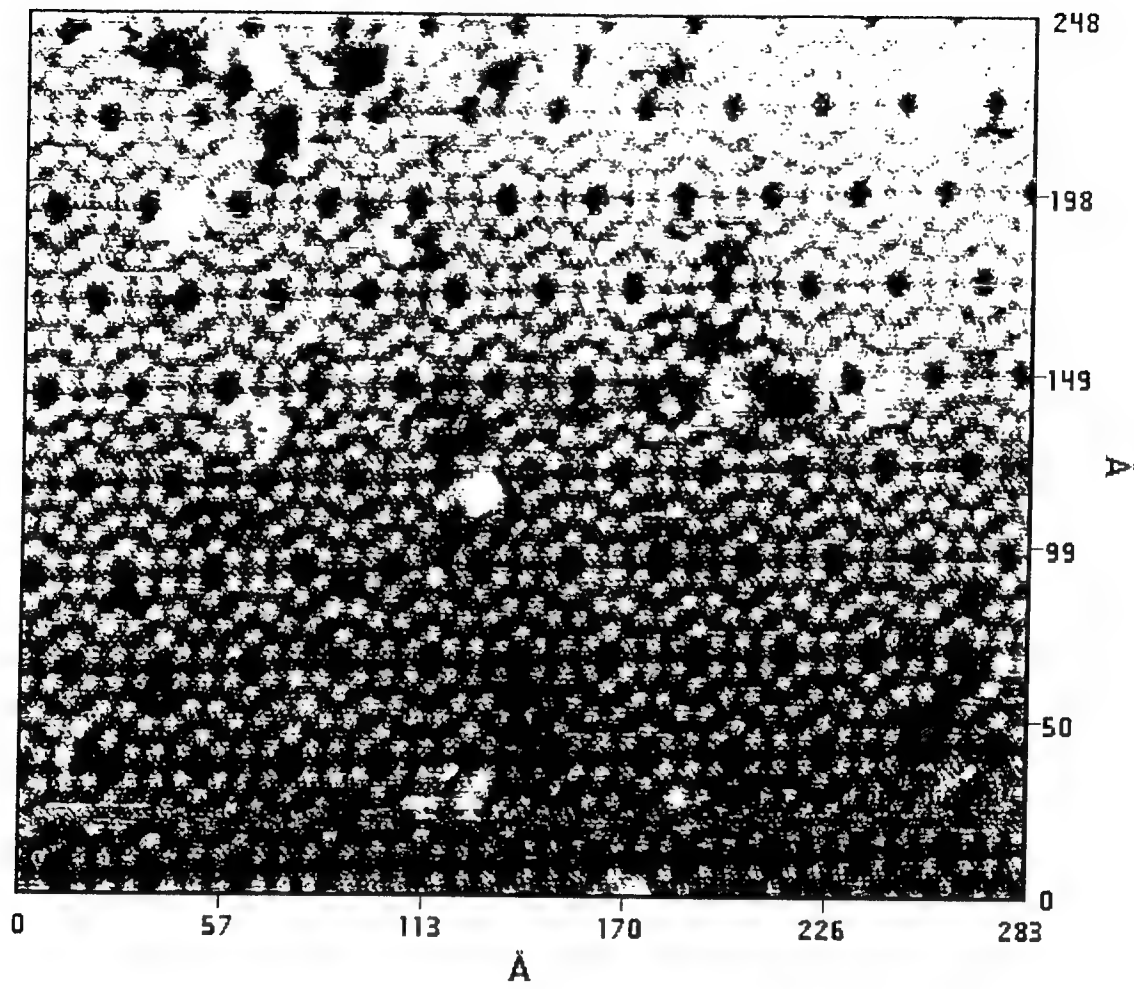


Figure 13: Constant current topographic image of the 7x7 Si(111) surface taken with all of the system's pumps in operation ( $I_{tip} = 1$  nA,  $V_{tip} = -2$  V).

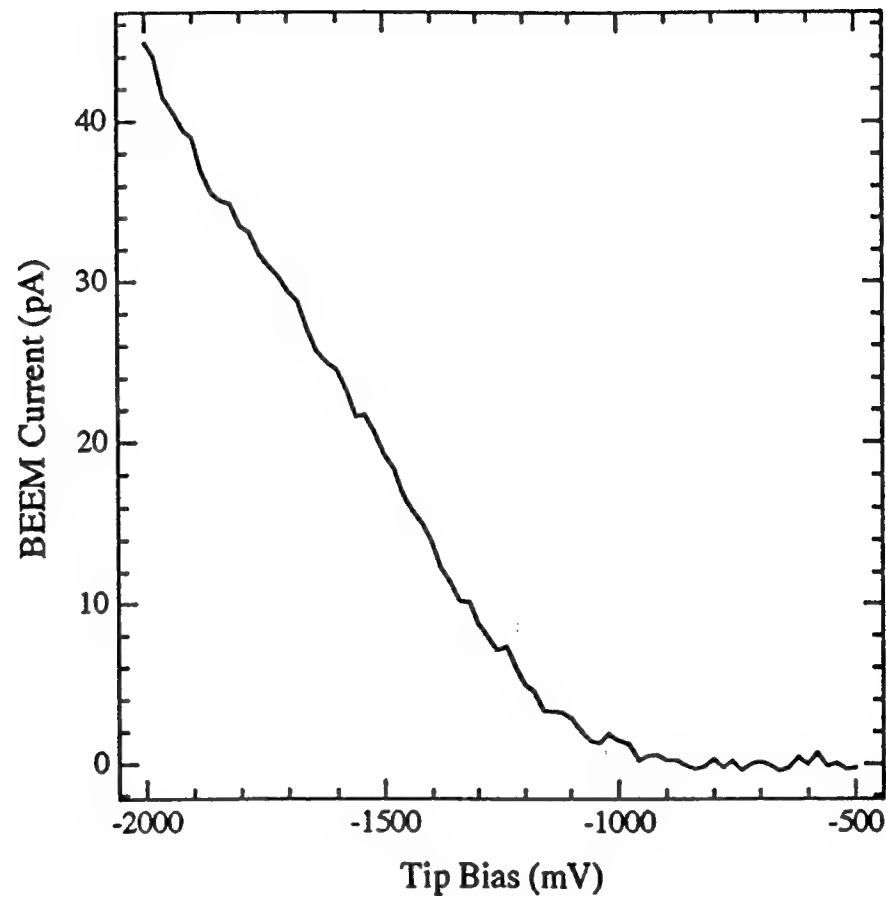


Figure 14: Averaged BEEM spectrum for a 2 nm PtSi/Si(111) n-type interface ( $I_{tip} = 1 \text{ nA}$ ).

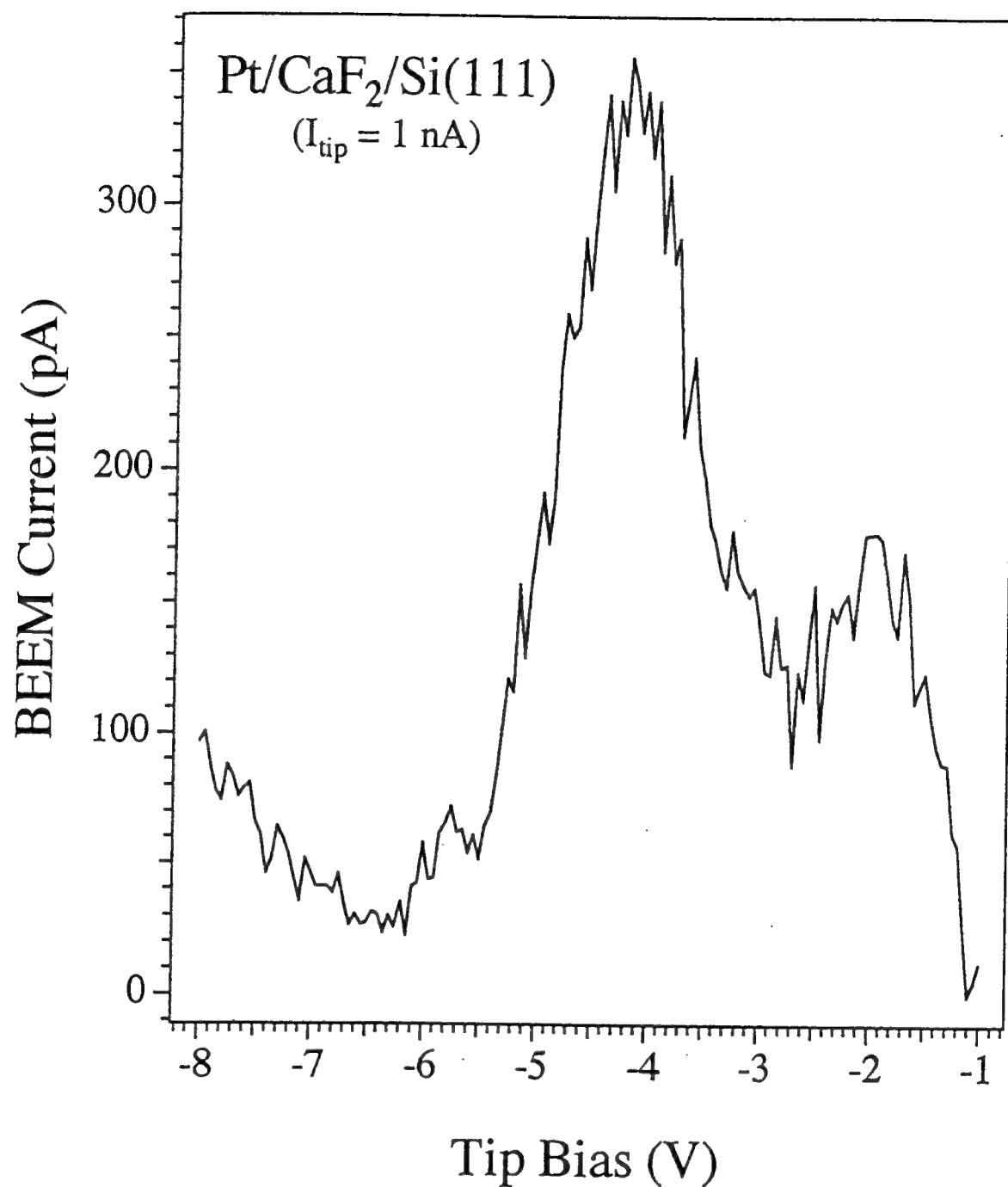


Figure 15: Averaged BEEM spectrum for a 2 nm Pt/ 0.6 nm CaF<sub>2</sub> / Si(111) n-type interface (I<sub>tip</sub> = 1 nA). Note that the spectrum appears to show resonant tunneling at a tip bias of -1.8 V which is below the CaF<sub>2</sub> conduction band at -3.5 V (i.e. 3.5 eV above the Pt Fermi energy).

## STM IMAGE

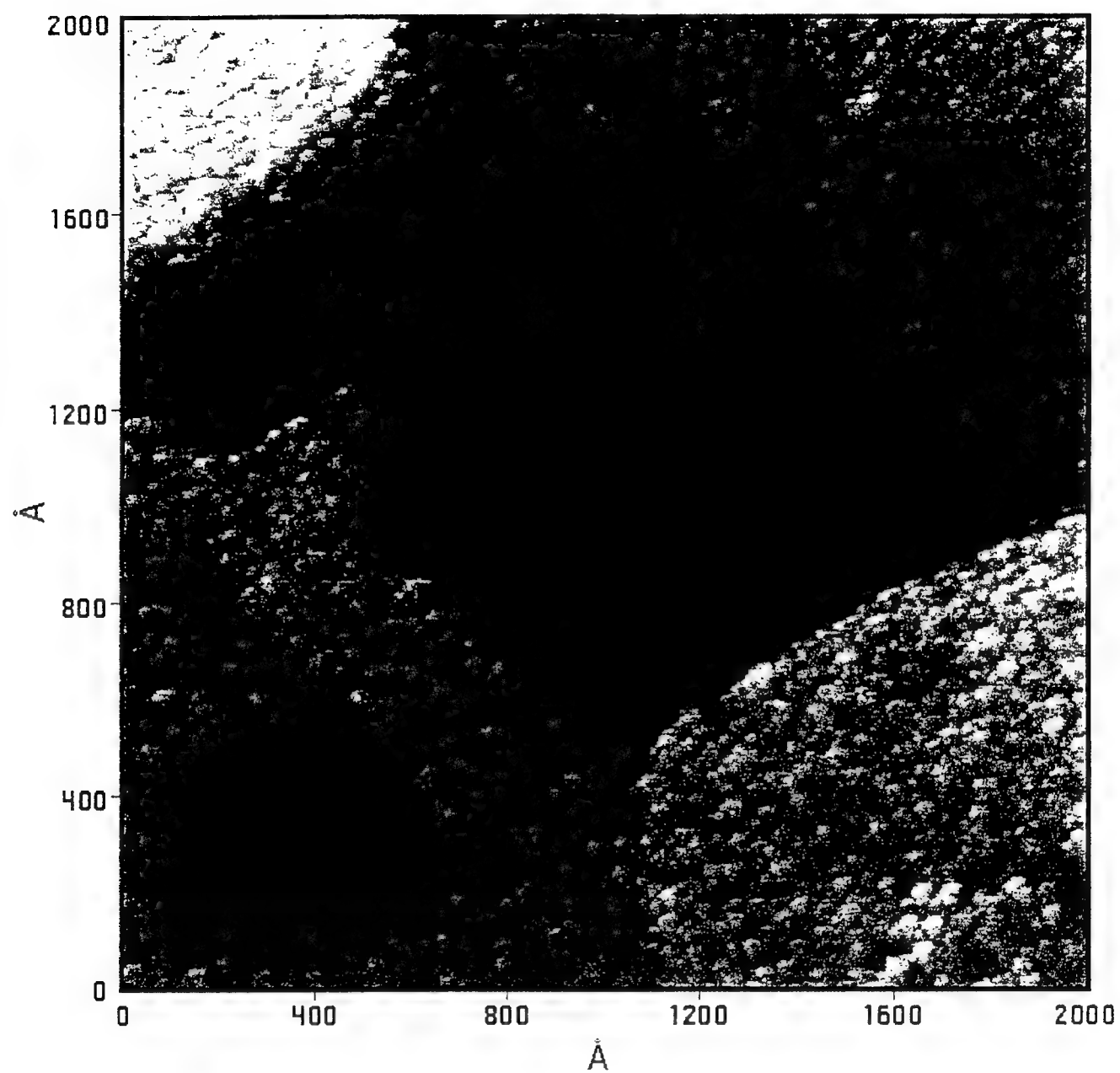


Figure 16: STM image of the 2 nm Pt/ 0.6 nm CaF<sub>2</sub> / Si(111) surface showing the nodules of Pt that appear on the as-deposited surface. In addition, the atomic steps in the underlying CaF<sub>2</sub> are clearly visible.

#### IV. Conservation of momentum parallel of the interface

We have demonstrated the fact that the quadratic threshold observed in BEEM spectroscopy and in internal photoemission spectroscopy may nothing to do with transverse momentum conservation at the M-S interface but can result simply as a consequence of the density of states of the semiconductor increasing as the square root of energy near a threshold. For the sake of clarity, we assume that the density of states in the metal is constant in the energy range near the threshold for BEEM current  $I_B$ , and we also neglect temperature effects (i.e., this is equivalent to assuming that the Fermi energy  $E_F$  is much bigger than  $kT$ ). An electron, which reaches the M-S interface with an energy  $E$ , is assumed to elastically scatter. The probability that it will scatter into a semiconductor state (and, thus, be detected as part of the BEEM current  $I_B$ ) is determined simply by the ratio of the number of accessible states in the semiconductor to the total number of accessible states in both the metal and the semiconductor. Thus,

$$I_B(V) \propto \int_0^{V-\Phi_S} dE \cdot n(E) \frac{g_s(E)v_s(E)}{g_m v_m + g_s v_s}, \quad (\text{IV.1})$$

where  $E$  is measured from the threshold in the conduction band (or valence band for holes),  $n(E)$  is the number density of electrons with energy  $E$  which reach the m/s interface, and  $g_i$  and  $v_i$  are the respective density of states and group velocities (perpendicular to the interface) of electrons in the semiconductor (s) or metal (m). Note that this expression neglects any dependence on the direction an electron is traveling when it reaches the interface since the scattering into final states is assumed to depend only on the initial energy of the electrons. Near threshold, when  $V - \Phi_S$  is small, this integral can be simplified by neglecting the energy dependence of  $n$ ,  $g_m$ , and  $v_m$  in favor of the much larger energy dependence of  $g_s$ , and  $v_s$  which both vary as  $\sqrt{E}$ , where  $E$  is measured from the minimum energy required to cross the Schottky barrier. Likewise,  $g_m v_m \gg g_s v_s$ . Thus,  $I_B(V) \propto (V - \Phi_S)^2$  very near threshold. As the tip voltage is increased, the energy dependence of the number density of electrons will have to be taken into account since this function should be peaked near the Fermi energy of electrons in the STM tip. This explains why the quadratic increase in the BEEM current observed near threshold rolls over into a linear increase in BEEM current at higher STM-tip biases.

It should be noted that this argument neglects quantum interference or quantum mechanical reflection (QMR) effects at the interface. While it is difficult to know exactly how to introduce these effects, Stiles<sup>1</sup> has indicated that QMR probably will contribute an additional 1/2 power dependence to the observed threshold behavior in analogy to the situation when scattering at the metallurgical interface is neglected<sup>2,3</sup>. It should also be noted that while neglecting the angular dependence of scattering is surely not physical, the fact that both no scattering at the M-S interface and complete scattering at this interface both give rise to quadratic thresholds in BEEM (and photoresponse) suggests that any more sophisticated model of scattering which takes into account some degree of transverse momentum conservation, is likely to result in the same threshold behavior.

## References for Section IV

- 1.) M. Stiles, private communication (1993).
- 2.) R. Ludeke and A. Bauer, Phys. Rev. Lett. **71**, 2224 (1993).
- 3.) G.N. Henderson, P.N. First, T.K. Gaylord, and E.N. Glytsis, PRL **71**, 2999 (1993)

## V. Monte-Carlo calculations of ballistic electron scattering

Ballistic-electron-emission microscopy (BEEM) is used to study the interfaces between metals and semiconductors. BEEM uses an STM tip to inject electrons (or holes, but here we will only use the word electron to refer to both types of single-particle charge excitations) into a thin metal sample. These electrons travel ballistically across the metal layer until they either: (i) lose enough energy to no longer be able to cross the Schottky-barrier into the semiconductor, or (ii) reach the interface and cross the Schottky barrier into the semiconductor. While traveling through the metal layer, the electrons can scatter elastically off phonons, defects, the interface, or the surface. Similarly, the electrons can lose energy through inelastic scattering events with other electrons or with appropriate defects, or with more energetic phonons. There are several interesting parameters which we wanted to model about this behavior. As is typical of Monte-Carlo (MC) modeling of ballistic transport in metal layers, we have chosen to model scattering in the metal layer as determined solely by an elastic scattering length and an inelastic scattering length. However, we were interested in how different initial momentum distributions (which is determined by the STM tip separation), and interface and surface scattering affected the electron transmission across the interface.

The program is written in C++ and can run either on a pc desktop computer or on the RS-6000 networked computers that we have at Rensselaer. The initial momentum distribution of electrons is computed analytically after which approximately  $10^6$  electrons are tracked in a MC calculation. For the more complex calculations (using actual Si band structure and assuming momentum conservation across the interface) the program will take up to 8 hours to complete a complete BEEM scan where the tip voltage is incremented from 0.8 V up to 1.5 V in 0.1V increments. We have modeled the probability that an electron incident on the interface will cross into the semiconductor in several different ways. In the nearly free electron model, the electron momentum and velocity are simply related to each other (through the effective mass of the electron) and it is assumed that the electron momentum parallel to the interface is conserved. We consider two other models which again both conserve crystal momentum parallel to the interface and again assume that the electrons in the metal are free-electron like. However, the actual band structure of the Si semiconductor is used. Since the projected electron minima are different for the (100) and (111) cases, quite different results are expected. Finally, we consider a model (referred to as the density of states model) where the momentum is not conserved across the interface. Instead, the probability that the electron crosses the interface is taken to be proportional to the number of accessible states in the semiconductor (as explained in Sec. IV above) divided by the total number of accessible states in both the metal and the semiconductor. We have also modeled the effects of electron reflection off the interface and surface (either

specular or diffusive) and the effects of strong inelastic scattering at one or the other of these surfaces.

This program was completed near the end of this project and while we have generated lots of data over the course of debugging it, there has not been much opportunity to explore different parameters with the final version of the program (earlier data suffered from an error in the band structure calculations of momentum conservation at the interface). In Fig. 17, a comparison of the (100), (111) and density of states model are compared when the tip is 0.5 nm for the sample, the elastic mean free path (mfp) is taken to be 13 nm, and the inelastic mfp is varied from 30 to 120 nm. The key thing to note is that the density of states calculation produces a quadratic threshold while the (111) orientation produces a much flatter curve which is not seen experimentally. We hope to use this data to demonstrate convincing evidence for strong elastic scattering at the metal/semiconductor interface.

Figure 18 shows typical MC calculations of BEEM currents at fixed voltage as a function of metal thickness. By varying the elastic and inelastic mfps, we can fit experimental data generated by our group and others. An important feature to note is that the apparent attenuation length changes as a function of metal thickness. This effect is due to the electron rattling off the front and back surfaces and is very sensitive to the type of scattering assumed at these interfaces.

$L_i = 30 \text{ nm}$  and  $L_e = 13 \text{ nm}$   
**For density of states, Si(001), and Si(111) models**

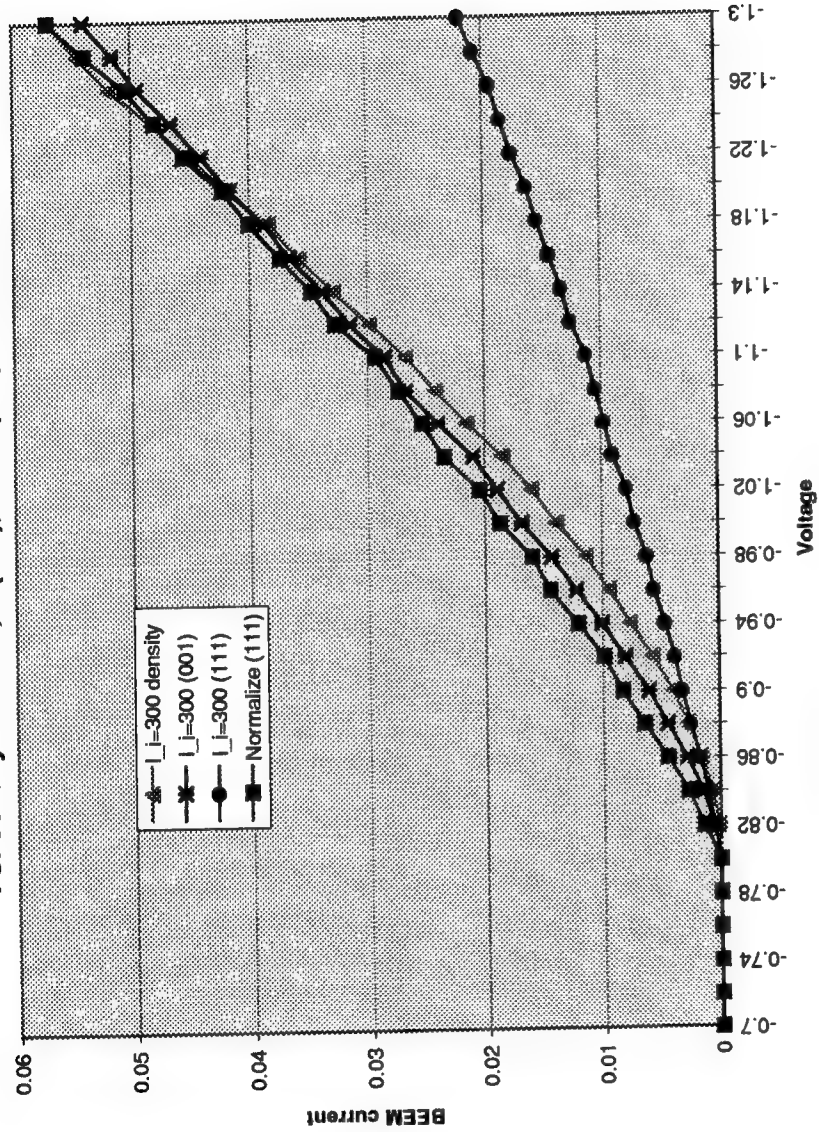


Figure 17: Three different MC calculations of the BEEM current (the so-called BEEM current is actually the ratio of the number of electrons which make it into the semiconductor over the total number of electrons which tunnel from the STM tip into the metal layer) as a function of tip bias are shown. For all three calculations, the elastic mfp  $L_e = 13 \text{ nm}$  while the inelastic mfp  $L_i = 30 \text{ nm}$ . The solid triangles represent the density of states (DOS) approximation (which assumes scattering dominates at the metal/semiconductor (m/s) interface) while the x's represent the assumption that parallel momentum is conserved at the m/s interface for a Si(001) orientation. In this case, the BEEM current is only slightly reduce from that of the DOS calculation (at voltages less than -1.2 V) and the voltage dependence is somewhat flatter. The solid circles again assume parallel momentum conservation but at a Si(111) interface. Since the BEEM current is substantially reduced for this orientation, the Si(111) data is also plotted normalized to the DOS approximation at -1.3 V. All calculated BEEM currents assume diffuse elastic scattering from the m/s interface and the front surface. In particular, the Si(111) BEEM current would be much smaller without this assumption.

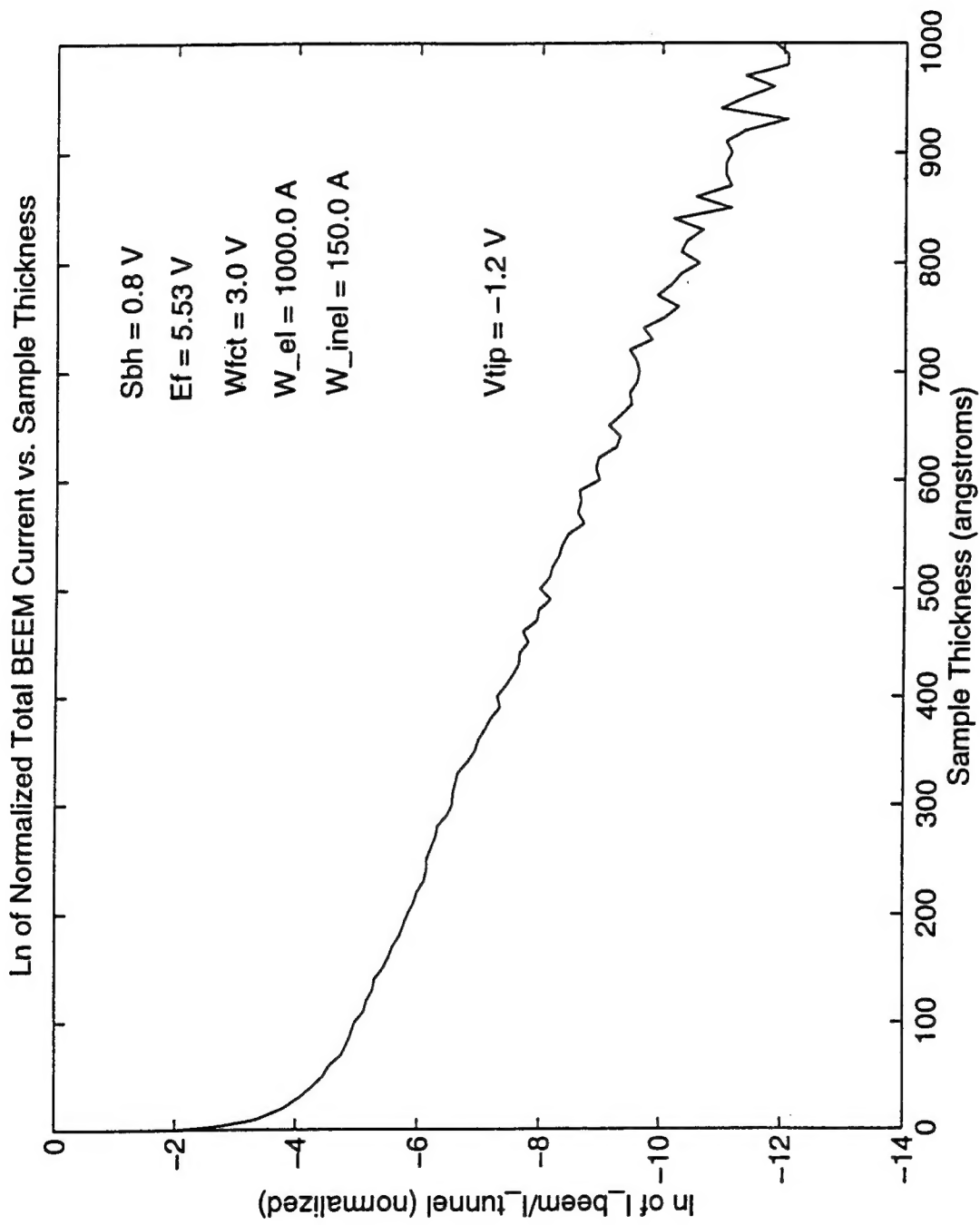


Figure 18: The natural log of the total BEEM current is plotted as a function of metal thickness while the tip bias is held constant at -1.2V and the tip separation is fixed at 0.5 nm. The apparent nonlogarithmic behavior of the BEEM current at thin metal thicknesses is due to electrons being able to rattle back and forth between the front and m/s interfaces.

### **Personnel Supported During this Contract:**

Dr. Leo J. Schowalter, professor in the Physics Department and Assoc. Director of the Center for Integrated Electronics and Electronics Manufacturing.

Dr. Carl Ventrice, post-doc and Visiting Assistant Professor in the Physics Department.

Mr. Vincent LaBella, graduate student.

In addition, we were awarded an AASERT award to this parent contract from AFOSR. This AASERT award was used to support Byong Kim. Dr. Kim is a US citizen and he successfully defended his Ph.D. thesis in July, 1996.

### **Ph.D. Thesis with AFOSR support through AASERT award and Air Force Support:**

"The effect of substrate misorientation on molecular beam epitaxial growth of thin CaF<sub>2</sub> film on Si(111) surfaces," B.M. Kim, Ph.D. thesis (Rensselaer Polytechnic Inst., unpublished, 1996).

### **Publications acknowledging Air Force:**

"MBE Growth of Thin CaF<sub>2</sub> Films on Vicinal Si(111) Surfaces," B. M. Kim, C. A. Ventrice, Jr., T. Mercer, R. Overney, and L. J. Schowalter, *Applied Surface Science* (1996).

"The effect of substrate misorientation on the evolution of surface morphology in epitaxially grown CaF<sub>2</sub>/Si(111) heterostructures," B.M. Kim, S.R. Soss, R.M. Overney, and L.J. Schowalter, *Mat. Res. Soc. Symp. Proc.* Vol. 399, p. 177 (1996).

"Measurement of Hot-Electron Scattering Processes at Au/Si(100) Schottky Interfaces by Temperature-Dependent Ballistic Electron Emission Microscopy," *Physical Review B* (1996).

"Hot-electron Scattering at Au/Si(100) Schottky Interfaces Measured by Temperature Dependent Ballistic Electron Emission Microscopy," *Applied Surface Science* (1996).

"Design of a scanning tunneling microscope for *in-situ* topographic and spectroscopic measurements within a commercial molecular beam epitaxy machine," C.A. Ventrice, Jr., V.P. LaBella, and L.J. Schowalter, submitted to *J. Vac. Sci., Technology* (1996).

"Dependence of Heteroepitaxial Growth on Substrate Misorientation: Nucleation of CaF<sub>2</sub> on Si(111) Surfaces," B. M. Kim, R. M. Overney, T. G. Thundat, and L. J. Schowalter, submitted to *Appl. Phys. Lett.* (1996).

### **Interactions/Transitions:**

Byong Kim and/or Leo Schowalter have presented the research work covered by this grant at the:

- *1995 March Meeting of The American Physical Society;*
- *Fifth International Conference on the Formation of Semiconductor Interfaces (ICFSI-5/June95);*
- *Gordon Research Conference, July, 1995;*

- the 1995 Fall Materials Research Society Meeting, Dec., 1996;
- the 1996 TMS Annual Meeting, Feb., 1996 (invited talk);
- the 1996 Spring Materials Research Society Meeting, April, 1996;
- the 1996 American Vacuum Society Meeting, Oct., 1996 (oral presentation scheduled).
- the 1996 Fall Materials Research Society Meeting, Dec., 1996 (oral presentation scheduled).

In addition, either Prof. Leo Schowalter, Byong Kim, or both have visited Rome Laboratories at Hanscom AFB to describe the current status of their work eight times during the life of this contract.

### **New discoveries, inventions and patent disclosures**

We have filed a patent disclosure entitled "Precise control, on a molecular level, of a epitaxial insulator across a large area substrate." This disclosure details the technique we have developed for growing precisely 2 monolayers of CaF<sub>2</sub> across almost all (except in regions where thick islands of CaF<sub>2</sub> are formed) of a large area substrate in spite of local fluctuations in the deposition rate. We claim that this technique will be useful for the formation of tunnel-barrier devices. Of particular interest for the Air Force on this contract, is the use of a tunnel-barrier to tailor the Schottky barrier in an infrared, Schottky-barrier detector. At the present time, it does not appear that Rensselaer will pursue patent protection on this invention.

## ***MISSION OF ROME LABORATORY***

Mission. The mission of Rome Laboratory is to advance the science and technologies of command, control, communications and intelligence and to transition them into systems to meet customer needs. To achieve this, Rome Lab:

- a. Conducts vigorous research, development and test programs in all applicable technologies;
- b. Transitions technology to current and future systems to improve operational capability, readiness, and supportability;
- c. Provides a full range of technical support to Air Force Material Command product centers and other Air Force organizations;
- d. Promotes transfer of technology to the private sector;
- e. Maintains leading edge technological expertise in the areas of surveillance, communications, command and control, intelligence, reliability science, electro-magnetic technology, photonics, signal processing, and computational science.

The thrust areas of technical competence include: Surveillance, Communications, Command and Control, Intelligence, Signal Processing, Computer Science and Technology, Electromagnetic Technology, Photonics and Reliability Sciences.